Applying flow cytometry to identify the modes of action of membrane-active peptides in a label-free and high-throughput fashion

Wichmann, Nanna; Lund, Philip M.; Hansen, Morten B.; Hjørringgaard, Claudia U.; Larsen, Jannik B.; Kristensen, Kasper; Andresen, Thomas L.; Simonsen, Jens B.

Published in:
B B A - Biomembranes

Link to article, DOI:
10.1016/j.bbamem.2021.183820

Publication date:
2021

Document Version
Peer reviewed version

Applying flow cytometry to identify the modes of action of membrane-active peptides in a label-free and high-throughput fashion

Nanna Wichmann, Philip M. Lund, Morten B. Hansen, Claudia U. Hjørringgaard, Jannik B. Larsen, Kasper Kristensen, Thomas L. Andresen, Jens B. Simonsen

PII: S0005-2736(21)00268-6

DOI: https://doi.org/10.1016/j.bbamem.2021.183820

Reference: BBAMEM 183820

To appear in: *BBA - Biomembranes*

Received date: 9 July 2021

Revised date: 29 October 2021

Accepted date: 12 November 2021

Please cite this article as: N. Wichmann, P.M. Lund, M.B. Hansen, et al., Applying flow cytometry to identify the modes of action of membrane-active peptides in a label-free and high-throughput fashion, *BBA - Biomembranes* (2021), https://doi.org/10.1016/j.bbamem.2021.183820

Applying flow cytometry to identify the modes of action of membrane-active peptides in a label-free and high-throughput fashion

Nanna Wichmann, Philip M. Lund, Morten B. Hansen, Claudia U. Hjørringgaard, Jannik B. Larsen, Kasper Kristensen, Thomas L. Andresen,* and Jens B. Simonsen*

Department of Health Technology, Center for Intestinal Absorption and Transport of Biopharmaceuticals, Technical University of Denmark, 2800 Kgs. Lyngby, Denmark

*Corresponding authors: tlan@dtu.dk and jbak@dtu.dk

Abstract: Membrane-active peptides (MAPs) have several potential therapeutic uses, including as antimicrobial drugs. Many traditional methods used to evaluate the membrane interactions of MAPs have limited applicability. Low-throughput methods, such as microscopy, provides detailed information but often relies on fluorophore-labeled MAPs, and high-throughput assays, such as the calcein release assay, cannot assess the mechanism behind the disruption of vesicular-based lipid membranes. Here we present a flow cytometric assay that provides detailed information about the peptide-lipid membrane interactions on single artificial lipid vesicles while being high-throughput (1000-2000 vesicles/s) and based on label-free MAPs. We synthesized and investigated six MAPs with different modes of action to evaluate the versatility of the assay. The assay is based on the flow cytometric readouts from artificial lipid vesicles, including the fluorescence from membrane-anchored and core-encapsulated fluorophores, and the vesicle concentration. From these parameters, we were able to distinguish between MAPs that induce vesicle solubilization, permeation (pores/membrane distortion), and aggregation or fusion. Our flow cytometry findings have been verified by traditional methods, including the calcein release assay, dynamic light scattering, and fluorescence microscopy on giant unilamellar vesicles. We envision that the presented flow cytometric assay can be used for various types of peptide-lipid membrane studies, e.g. to identify new antibiotics. Moreover, the assay can easily be expanded to derive additional valuable information.

1. Introduction

Membrane-active peptides (MAPs) have potential applications in biotechnology [1,2], particularly within

therapeutics [3–5]. Some MAPs are, for example, antimicrobial peptides (AMPs) that show antimicrobial activity through pore formation in lipid membranes [4,6–8]. These AMPs are receiving increased attention, as pathogenic microorganisms are becoming increasingly resistant towards conventional antibiotics [9]. Another interesting therapeutic application of MAPs is their use as cell-penetrating peptides (CPPs). Introducing a CPP moiety to a drug can improve or facilitate drug internalization through biological membrane barriers [10–14]. In general, peptides are interesting from a drug development perspective, because automated solid-phase peptide synthesis allows for high-throughput synthesis of peptides with variations in the amino acid sequence and/or containing amino acid modifications.

To rationally engineer MAPs for therapeutic applications, it is critical to understand the modes by which they interact with lipid membranes. Current approaches often rely on fluorophore-labeled peptides, which, combined with low-throughput fluorescence microscopy, can provide detailed mechanistic information [15]. However, fluorophore-labeling of peptides can dramatically alter the mode of membrane interaction of the peptides [16]. Many traditional fluorophore-labels have been shown to have a significant affinity towards the lipid membranes [17,18]. Further, the evaluation of therapeutic peptides from large peptide libraries can be a rate-limiting factor in the identification of lead drug candidates due to lack of high-throughput evaluation assays. High-throughput methods that rely on label-free peptides are often limited in revealing mechanistic insights about how MAPs interact with membranes. Among high-throughput assays, the calcein release assay is likely the most commonly used to study lipid membrane perturbations, induced by external agents such as MAPs [1,16,19–22]. This assay relies on the appearance of calcein fluorescence after release from the core of artificial (lipid) vesicles (in the following denoted ‘vesicles’). As in many other studies, the vesicles represent a simple model system of cell membranes [21,23–26]. However, the calcein release assay falls short in providing mechanistic information, as it cannot distinguish whether MAP-mediated calcein release is due to vesicle solubilization or localized membrane permeabilization. In addition, it provides no information about vesicle fusion and aggregation, two phenomena that potentially also may lead to calcein release independent of the direct membrane

perturbations and, thereby, putative biological activity of the peptides [27].

To overcome some of the limitations associated with the most commonly used methods for studying peptide-lipid membrane interactions, we developed a method based on flow cytometry. A flow cytometer is a microfluidic system equipped with several lasers and corresponding detectors that allow for high-throughput multi-parameter analysis of single particles in terms of their light scattering and fluorescence properties. Properties that can be used to phenotype cells by using fluorophore-labeled antibodies against antigens on specific cell types [28]. Flow cytometry has previously been used to investigate the interactions of MAPs with cells, for example, mapping the time course of AMP-induced permeabilization of bacteria using live/dead DNA-probes [29] and the cell-penetration properties of CPPs fused with GFP [30]. In the latter study, additional microscopy studies were needed to verify that the CPP-GFP compounds were able to penetrate into the cell. A general limitation of traditional flow cytometry is its inability to directly assess whether compounds of interest are at the cell surface or inside the cell [31].

Conventional flow cytometers can also be used to study submicron vesicles [32–34]. In this study, we determined how flow cytometry on dual-fluorophore-labeled vesicles (a core- and a membrane–fluorophore) can be used to study the membrane interactions of label-free MAPs. The concept is shown in Figure 1, and exemplified by a MAP that leads to pore formation in the vesicle membrane. By using the fluorescence intensity from the membrane-fluorophore as an indirect measure of the vesicle size-integrity in combination with an indirect measure of the vesicle concentration, we could determine whether peptide-dependent reduction in the core fluorescent readout was due to localized membrane permeabilization or vesicle solubilization. In the former case, the vesicle concentration and fluorescence intensity from the membrane fluorophore is unchanged, whereas in the latter case, the vesicle concentration and fluorescence intensity from the membrane-fluorophore decreases. Finally, increases in the membrane fluorescence for individual readouts reveal MAP-induced vesicle fusion/aggregation. Based on the above, we present a flow cytometry assay that provides an integrated platform to study the membrane interactions of peptides on a single vesicle level in detail in a label-free and high-throughput manner.

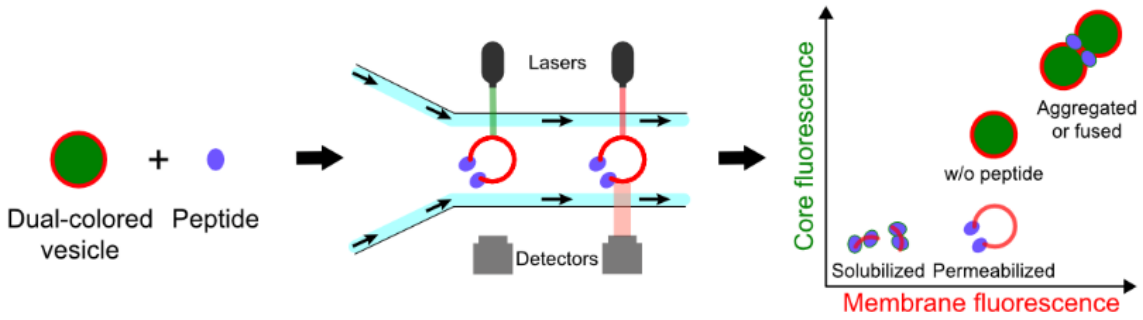

Figure 1: Concept – applying flow cytometry to identify MAPs' modes of action. The different steps in the peptide-lipid membrane interaction assay. Left: the vesicle-peptide reaction. The red color on the vesicle refers to membrane-anchored fluorophores, and the green color represents the core-fluorophores. Center: The flow cytometry measurement of the reaction mixture. A MAP that induces pore formation in a vesicle is shown – the released core-fluorophore is heavily diluted and thus not shown. Right: The analysis that provides general information on the MAP's mode of action. We can identify the three modes of action: (i) Leakage due to localized membrane permeabilization, (ii) leakage due to membrane solubilization, and (iii) vesicle aggregation/fusion.

To evaluate the versatility of our flow cytometric assay, we synthesized six MAPs. Five of the MAPs are well-studied with respect to their membrane interactions, and one is the potent pore-forming peptide macrolittin-70 developed recently [25]. The five known MAPs include the three AMPs melittin [35,36], magainin-2 [37,38], and LL-37 [39], and the two highly cationic CPPs penetratin [40,41] and HIV-derived peptide Tat [42,43]. These MAPs are known to exhibit different modes of action, including membrane permeabilization [3] and membrane solubilization [44,45]. Further, we envision that the highly positively charged CPPs could lead to vesicle aggregation or fusion in membrane-assays when negatively charged vesicles are applied [27].

We verified the flow cytometry findings with data from (i) the traditional high-throughput calcein release assay that measures calcein escape from vesicles, (ii) dynamic light scattering (DLS) that measures the

apparent size of the vesicles, and (iii) visual-based fluorescence microscopy studies on giant unilamellar vesicles (GUVs).

2. Results and discussion

2.1 Dual-labeled vesicles used as membrane model in the flow cytometry assay

Previous research have shown that vesicles can be studied by flow cytometry when the membrane of the vesicles is fluorophore labeled [32,33,46,47]. Therefore, in this study, we prepared large vesicles (LVs) containing 1 mol% of a DOPE lipid conjugated to Atto655 as membrane label (membrane-fluorophore), 20 mol% of the negatively charged POPS lipid to prepare vesicles with an overall net negative membrane charge like biological membranes, and 79 mol% POPC (one of the most commonly used lipids in vesicle studies). In order to detect changes in the barrier properties of the vesicle membrane, we encapsulated the small fluorescent dye Alexa488 inside the core of the vesicles (core-fluorophore). We used an appropriate core-fluorophore concentration of 80 μM that was adequate for detection by flow cytometry without eliciting quenching (Figure S1 in the Supplementary information (SI)).

The LVs were prepared with diameters spanning between 100-1000 nm using a standard lipid film rehydration method [48]. In brief, the mixed lipid films were hydrated in a phosphate buffer (10 mM phosphate, 100 mM NaCl, pH 6.7) containing 80 μM core-fluorophore, freeze-thawed five times, and extruded five times through a 400 nm pore filter followed by size-exclusion chromatography to remove the non-encapsulated core-fluorophore. This preparation method was expected to yield a polydisperse sample of LVs. As a negative control for LVs containing the core-fluorophores, we prepared LVs without core-fluorophore by hydrating the lipid film in the bare buffer.

Classical ensemble/bulk-based characterization techniques such as DLS are not well suited for a study of the size distribution of polydisperse samples or samples containing multiple size populations [49–51]. Along this line, it was not possible to obtain reproducible size populations from DLS measurements (data not shown). Hence, to validate the size distribution of the LVs, we used nanoparticle tracking analysis (NTA), a single-particle characterization tool that tracks the Brownian motion of individual particles in suspension to determine particle size (Figure 2). Due to its sensitivity and robustness to determine

concentration and size distribution of polydisperse, sub-micron particles, NTA has become the gold standard for characterization of the biological vesicles known as extracellular vesicles [52]. With our NTA setup, we were able to track the LVs by one of the following three tracking modes: Light scattering (640 nm), fluorescence from the core-fluorophore (excitation 488 nm, detection > 500 nm), and fluorescence from the membrane-fluorophore (excitation 640 nm, detection > 660 nm). NTA analysis based on scattering demonstrated that the LVs had a mean diameter of 207 nm and a standard deviation (SD) of the population of 98 nm. The large SD highlights the significant size-heterogeneity of the LV sample. The presence of LV sizes above 400 nm, which is the size of the membrane pores used for extrusion, could be due to defects in some of the pores (we only extruded the LV samples five times) and that larger sized vesicles are modular/flexible and thus able to squeeze through pores smaller than the LVs. Further, studies have shown that LVs formed by rehydration, cycles of freeze-thawing, and extrusion can form LV populations with mean sizes below the pore size of the membrane used for extrusion when the pore size is above 100 nm [33,53]. The size distributions derived from tracking LVs using the membrane-fluorophore fluorescence and core-fluorophore fluorescence overlay well with the scatter-based size distribution, with mean ± SD sizes of 241 nm ± 113 nm and 226 nm ± 90 nm, respectively. The slight discrepancies between the derived mean sizes may be due to different optical sensitivities and settings of the tracking modes. Furthermore, the vesicle concentrations detected by using the three different detection modes are similar (3-5 x 10^{11} particles/mL). Together, the NTA data confirm that we have prepared LVs containing both core-fluorophore and membrane-fluorophore. We also prepared LVs without core-fluorophore. These have a size distribution based on light scattering that was approximately the same (mean ± SD size of 204 ± 90 nm) as the dual-labeled LVs (Figure 2B). The size distribution based on the membrane-fluorophore fluorescence was slightly larger (mean ± SD size of 281 ± 141 nm). However, in contrast to the dual-labeled LVs, we detected significantly fewer events from the LVs without core-fluorophore when we tracked the LVs using the fluorescence detection used for the core-fluorophore fluorescence, as expected. Together, the NTA data support that we have prepared LVs with sizes and fluorophore-labels that are suitable for flow cytometry.

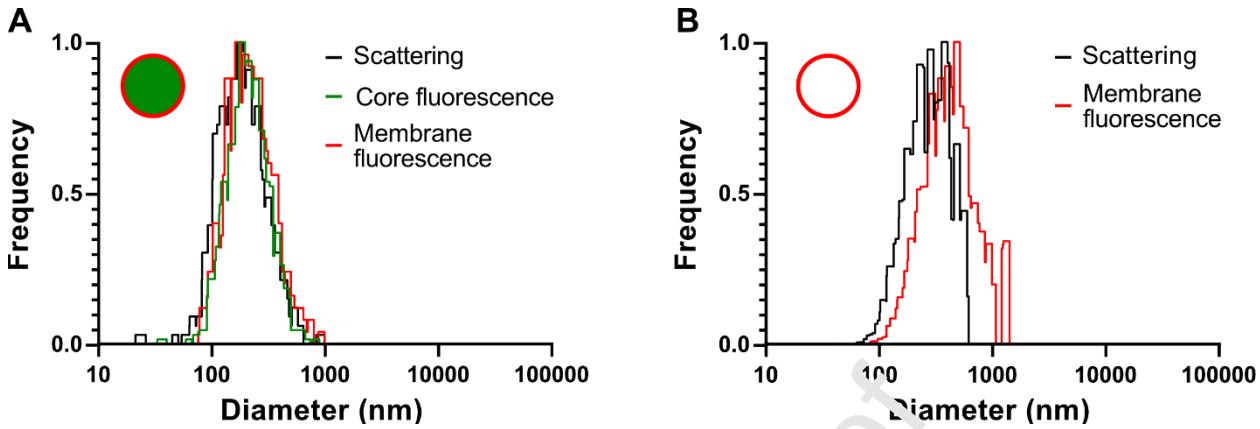

Figure 2: Size distribution of the LVs. The size distribution of LVs with core-fluorophore (A) and without core-fluorophore (B) derived from NTA measurements. The size distributions are shown for each of the relevant detection modes: Light Scattering (black line), core-fluorophore fluorescence (green line), and membrane-fluorophore fluorescence (red line). The inserted circles illustrate the LVs including the position of the fluorophore-labels and their fluorescent colors.

2.2 Detecting LVs by flow cytometry

To correlate MAP activity with the fluorescence signal in flow cytometry, it was a prerequisite that the dual-labeled LVs could be detected by the flow cytometer and distinguished from the LVs without core-fluorophore. Therefore, we adjusted the vesicle concentration and flow cytometry settings to enable the detection of single LVs by flow cytometry. We triggered the detection of the LV events based on the fluorescence from the membrane-fluorophore in line with previous studies [33]. Using a trigger (threshold) value of 200 arbitrary 'membrane fluorescence intensity' units (AU) gave rise to 800-2300 events per second, of which the bare buffer or non-membrane labeled LVs only accounted for ≤ 1% of the total count. Therefore, the recorded events for the samples can be considered to be primarily membrane-labeled LVs.

We most likely only detected the largest LVs due to the limited sensitivity of the flow cytometer, and thus, we obtained a membrane-fluorophore fluorescence profile of the LVs (Figure 3A) that peaks (is cut off) at

the threshold value (200 AU). Although we were not able to detect the entire LV population, it is important to note that our assay is not dependent on measuring all LVs. The membrane-fluorophore fluorescence intensity profiles and median fluorescence intensity (MFI) based on the membrane-fluorophore fluorescence (membrane MFI) for the LVs with (membrane MFI = 287 ± 2 AU) and without core-fluorophore (membrane MFI = 293 ± 3 AU) are almost identical, which confirms their similar size distribution derived from NTA (Figure 2). To ensure that we study individual LVs, we performed an LV dilution series, which is commonly used to optimize the study of individual EVs by flow cytometry [54]. We used an LV lipid concentration (500 nM) that was within the concentration regime that shows a linear correlation between the count rate and the particle concentration, and a constant membrane MFI and fairly constant core MFI (Figure S2 in SI), and this strongly supported that we mostly detect single LVs [34,54].

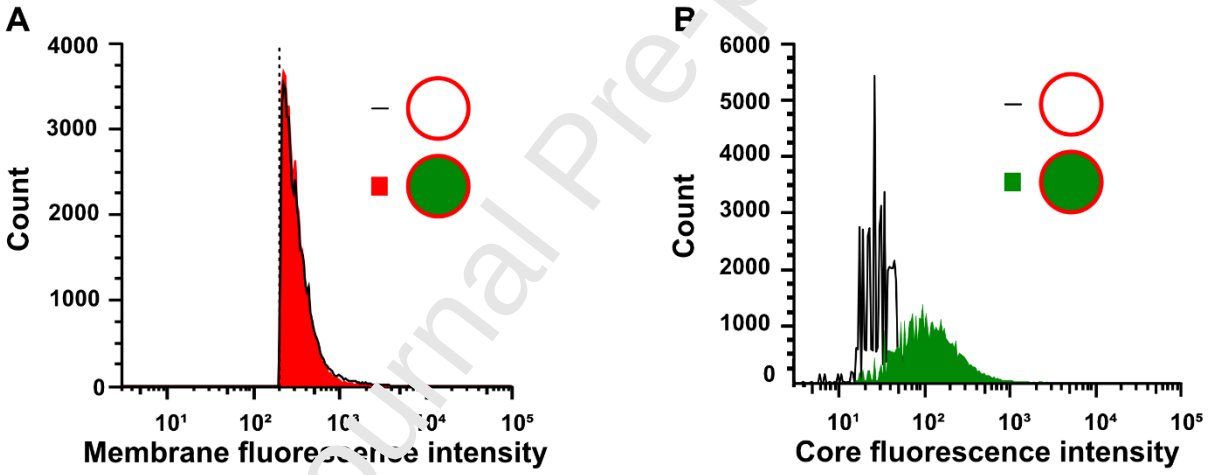

Figure 3. Flow cytometry data on LVs. Representative histograms based on fluorescence from the membrane-fluorophore triggered at 200 AU (A, membrane fluorescence intensity) and the core-fluorophore (B, core fluorescence intensity) of LVs with (filled, colored) and without (black line) the core-fluorophore. The circles illustrate the LVs, including the position of the fluorophore-labels and their fluorescent colors. The black dotted line in A marks the trigger threshold value. The fluorescence intensities are in AU.

We plotted the core-fluorophore fluorescence intensity profiles of LVs with or without core-fluorophore,

both triggered by the membrane-fluorophore fluorescence (Figure 3B). It is clear from the profiles and the corresponding MFI values of the LVs with (104 ± 3 AU) and without core-fluorophore (28 ± 2 AU) that these two different LV samples can be clearly distinguished based on their core MFIs. The symmetric profile of the core-fluorophore fluorescence of the dual-labeled LVs is different from the membrane-fluorophore fluorescence-based profile. The different profiles may in part be due the core fluorescence signal being processed differently to the trigger channel (membrane fluorescence) and some detector variation, and in part due the fact that the membrane fluorescence scales with the area, and the core-fluorescence scales with the volume of the LV. The impact on the triggering strategy was also present when we triggered the LVs on the core-fluorophore; we observed a symmetric membrane-fluorophore fluorescence intensity profile and an asymmetric core-fluorophore fluorescence intensity profile (Figure S3 in SI). Since we can detect single LVs with and without core-fluorophores, we have the appropriate LV samples and flow cytometry settings in place to study the interaction of MAPs with LV membranes. Importantly, we also tested that the fluorescence readouts from the LVs were constant within the timeframe used for the MAP-LVs studies (Figure S4A and B in SI).

2.3 Synthesis of MAPs

Having established that we can detect the LVs using flow cytometry based on their membrane-fluorophore fluorescence, and distinguish similar LVs with and without core-fluorophore, we aimed to study the effect of peptides on the LVs. For this, we synthesized the MAPs LL-37, melittin, magainin-2, macrolittin-70, Tat, and penetratin (Figure 4), covering a range of different MAP-membrane interactions including membrane permeabilization, membrane solubilization, and potentially also vesicle aggregation.

All the peptides were prepared by microwave-assisted solid phase peptide synthesis using standard protocols [55]. Briefly, the peptides were synthesized on PAL-AM resin, TentaGel S RAM resin, or a preloaded Wang resin with diisopropylcarbodiimide as coupling reagent, and Oxyma as auxiliary nucleophile. After the final coupling and Fmoc removal, the peptides were cleaved and globally deprotected in trifluoroacetic acid, precipitated in diethyl ether, and purified by high-performance liquid chromatography (HPLC). Identification and purity of the peptides were assessed by mass spectrometry

and analytical HPLC, respectively, see Figure S10-S21 in SI.

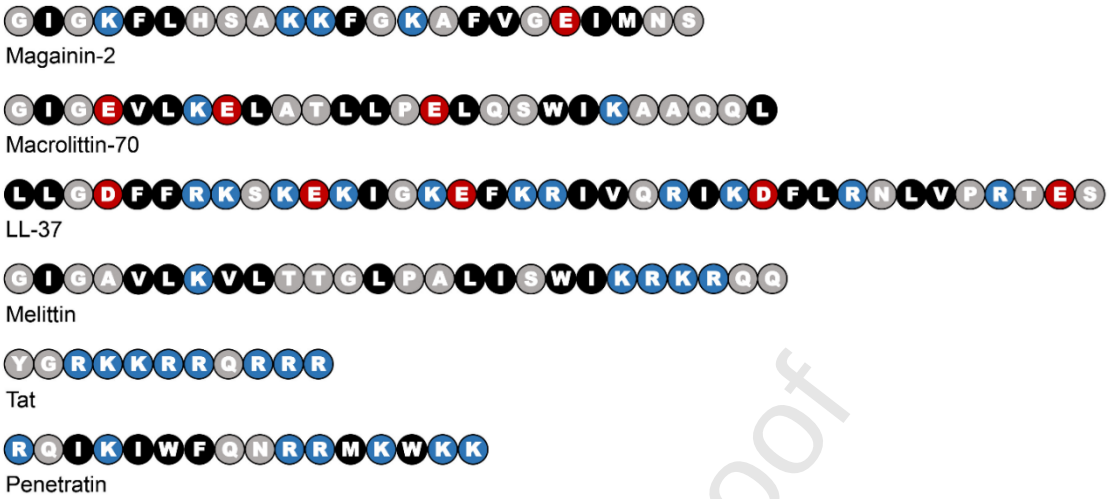

Figure 4. Amino acid sequence of the synthesized membrane-active peptides (MAPs). Primary sequences, as described using the one letter code, of the MAPs used in this study. Hydrophobic residues are colored black, anionic residues red, cationic residues blue, and all other residues grey. Some of the MAPs are modified in the N- and C-terminus (see Materials and methods section). The anionic and cationic classifications of the residues are based on their expected overall charge at the pH condition used in this study (pH 6.7).

2.4 Identifying different types of peptide-lipid membrane interactions

To identify different kinds of peptide-lipid membrane interactions, we mixed each of the six synthesized MAPs with LVs with core fluorophore to a final MAP concentration of 10 μM and a final LV lipid concentration of 50 μM. The mixtures were incubated at 37˚C for 30-60 min to give the MAPs time to interact with the LVs. Subsequently, the solutions were diluted to a final lipid concentration of 500 nM so it was in the range for single LV detection by flow cytometry.

For magainin-2, macrolittin-70, LL-37, and melittin, the core MFI dropped from 104 ± 4 AU without MAP to 33-39 AU after incubation, which is similar to the core MFI for the LVs without core-fluorophore (core MFI = 28 ± 2 AU) (Figure 5A). These data show almost complete release of the core-fluorophore when the LVs were exposed to these MAPs. The observations are consistent with these four peptides

being known to induce a release of core-content from vesicles [3,24,44,56]. For Tat and penetratin, the core MFI increased about two-fold (Figure 5A). This was likely due to a peptide-induced aggregation of the anionic LVs, as penetratin and Tat are both highly positively charged at the pH level used in this study (pH 6.7), as illustrated in Figure 4. While it should be emphasized that the flow cytometry assay cannot distinguish between LV aggregation or fusion, previous studies support the notion that highly positively charged peptides can form aggregations of negatively charged vesicles [57,58].

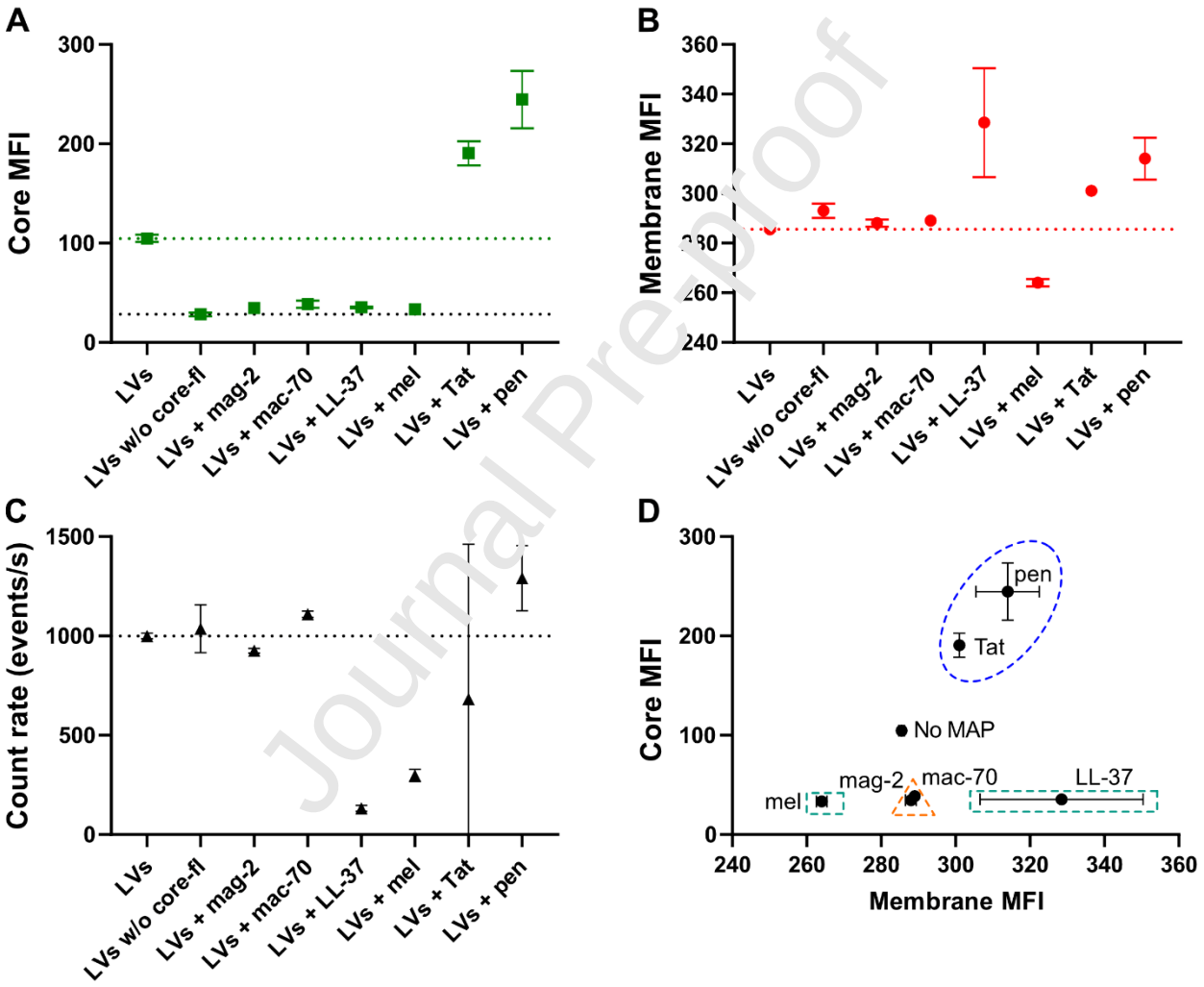

Figure 5. Flow cytometry measurements of LVs in the absence and presence of MAPs. Core MFI (A), membrane MFI (B), and count rate (C) for LVs with core-fluorophore in absence (LVs) or presence of MAPs (LVs + MAP) as well as for LVs without core-fluorophore (LVs w/o core-fl). (D) Scatter plot based on the membrane and core MFI values, with each point being labeled with the respective MAP.

MAPs leading to core-fluorophore release without solubilization are marked with an orange triangle, MAPs leading to core-fluorophore release and solubilization are marked with a turquoise square, and MAPs leading to aggregation of the LVs are marked with a blue circle. The shown data are averages of two replicates and their standard deviation. mag-2: magainin-2, mac-70: macrolittin-70, mel: melittin, pen: penetratin. The MFI values are in arbitrary units.

To investigate the state of the LV membrane upon reaction with the MAPs, we studied the membrane MFI (Figure 5B). The membrane MFI of the LVs did not differ much for the LVsexposed to magainin-2, macrolittin-70, or no MAP. This supports the interpretation that these MAPs led to increased membrane permeability without disrupting the LVs with respect to size, which is consistent with these MAPs forming pores as shown in the literature [3,59]. For melittin, however, the membrane MFI dropped, and for LL-37, the membrane MFI increased, indicating that the membrane was affected. In agreement with this, the count rate was almost unaffected for the LVs that were exposed to magainin-2 or macrolittin-70, and it decreased dramatically for the LVs that were exposed to LL-37 or melittin (Figure 5C). This corroborates earlier finding using bulk assays [44,45] and suggests that LL-37 and melittin solubilize the membrane of a majority of the LVs. Ladokhin and White [45] found that melittin functions in a detergent-like manner for anionic vesicles which supports our flow cytometry findings. For LL-37, the solubilization is consistent with the study by Sancho-Vaello et al. [44]. The increased membrane MFI with a dramatic drop in core MFI and drop in count rate could be a result of the LL-37 forming a few large aggregates with the membrane-fluorophore. It should be mentioned that LL-37 is a large amphipathic peptide comprised of 37 amino acids (Figure 4). Hence, it is likely that it can form large LL-37-lipid aggregates.

For Tat and penetratin, both the core- and membrane MFI increased, supporting LV aggregation or fusion mediated by these highly cationic peptides (Figure 5A and B). The corresponding count rate data may at first glance contradict our aggregation/fusion interpretation as the count rate clearly increased in the penetratin case (Figure 5C). However, since we only detected a fraction of the LVs, the LVs that

otherwise go undetected could, if they aggregate of fuse, get above the triggering threshold and thus add to the total count rate. The count rate data on Tat varied a lot (Figure 5C). We therefore performed a separate quadruplicate flow cytometry study on Tat that clearly showed that the count rate of LVs + Tat was also increased compared to the bare LV control (Figure S5 in SI) like in the penetratin case. Hence, all the measurable parameters support the assumption that highly positively charged peptides like Tat and penetratin likely form aggregates with the negatively charged LVs, and that they do not permeabilize the LVs.

To assign the mode of action for a given MAP, we plotted the core and membrane MFI values from the LVs as a scatter plot in Figure 5D. This plot, together with the measured count rates, can help assign MAPs to the various known modes of action, including membrane permeabilization, membrane solubilization, and vesicle fusion/aggregation. To ensure that our findings were reproducible on a day-to-day basis, we conducted the same kind of measurement on other days and got similar results (Figure S4C-E in SI). We also showed that working at higher LV concentrations, i.e., studying a significant proportion of co-particle events, also lead to the same assigned modes of action (Figure S6 in SI). The latter condition obviously gave rise to a higher signal, which can be useful if the signal-background resolution is low when studying single LV events. Along these lines, it is important to emphasize that the choice of LVs in terms of size and degree of fluorophore-labeling used for the flow cytometric assay depends to some extent on the sensitivity of the flow cytometer being used. To investigate whether attractive electrostatic interactions play a role in the formation of LV aggregates/fusion, we performed a head-to-head experiment with Tat exposed to the negatively charged LVs containing POPS (the LVs used so far), and to neutral LVs without the negatively charged POPS (Figure 6A). The relatively high membrane MFI value measured for the Tat-anionic LV mixture indicates that Tat forms larger aggregates with the negatively charged LVs than with the neutral LVs. It is known that LVs comprised of only zwitterionic phosphatidylcholine lipids (like in our case) are slightly negatively charged. This small negative surface might be enough for Tat to mediate some aggregation/fusion. Corresponding data based on the core-fluorophore supports that Tat forms the largest aggregates with the anionic LVs (Figure S7A

in SI).

Previous studies have shown that magainin-2 induces permeabilization in negatively charged vesicles, but not in neutral vesicles [60,61]. We confirmed these findings using the flow cytometric assay (Figure 6B). It is clear that magainin-2 led to a decrease in the core MFI only for the negatively charged LVs. The complementary membrane-fluorophore data supports the interpretation that the decrease in core MFI is not due to solubilization of the LVs (Figure S7B in SI).

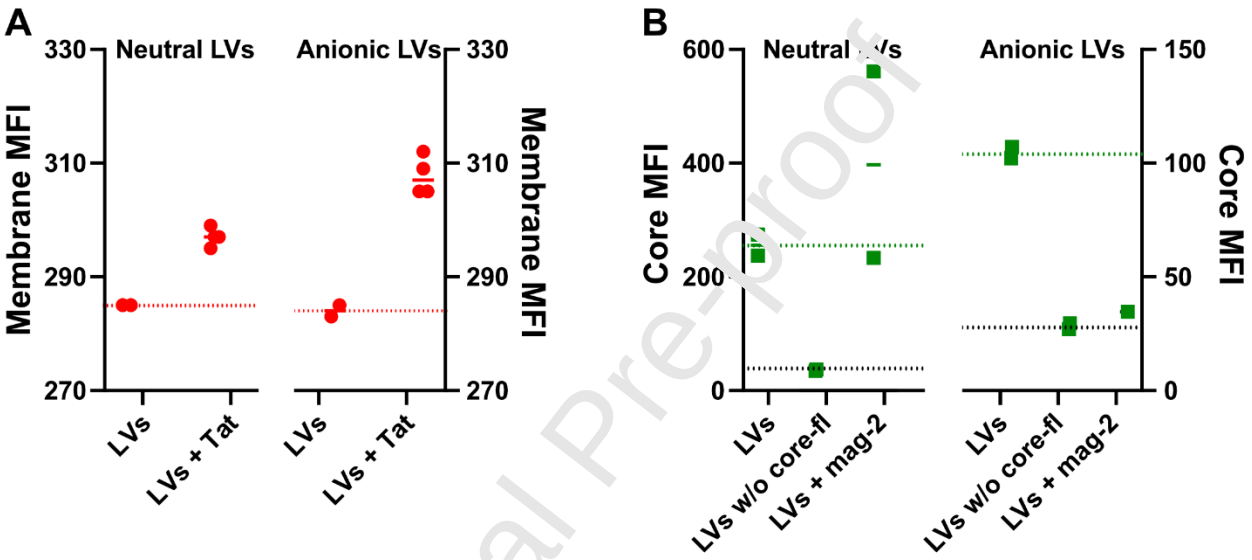

Figure 6. Distinguishing MAP effects on neutral and anionic LVs. Membrane MFI (A) and core MFI (B) for LVs with core-fluorophore in absence (LVs) or presence (LVs + MAP) of a MAP, as well as for LVs without core-fluorophore (LVs w/o core-fl). The membrane of the LVs are either neutral (left) or negatively charged (right) in both (A) and (B). The short solid colored lines represent the average of the shown MFIs for LVs exposed to a MAP. The dotted, colored lines show the average of the MFI for the neutral and charged LVs in the absence of a MAP. The dotted black lines are the average of the MFI for the neutral and charged LVs w/o core-fl. The MFI values are in arbitrary units.

We have successfully developed a flow cytometer assay that allowed us to distinguish between peptides that: (i) led to increased membrane permeability without solubilization (magainin-2 and macrolittin-70), (ii) led to solubilization of the LVs and release of core-fluorophore (LL-37 and melittin), and (iii) did not

lead to core-fluorophore release, but rather aggregation of the LVs (Tat and penetratin) (Figure 5D). In its current form, our assay cannot assess whether translocation of the CPPs Tat and penetratin takes place. Rather, our data highlight potential interactions or artifacts in peptide-lipid membrane studies when we use highly positively charged peptides in combination with negatively charged LVs.

It should be noted that the flow cytometric assay based on non-fluorophore-labeled MAPs have a few other limitations: It does not distinguish between MAPs that do not bind to LVs on the one hand, and MAPs that do bind and/or penetrate the LV membrane but do not lead to (i) release of the core-fluorophore (ii) and/or fusion and aggregation of LVs on the other. One way to overcome this binding issue is to fluorophore-label the MAP. One key feature of flow cytometry is its ability to analyze multiple different fluorescence parameters on single particles. Conventional flow cytometers can simultaneously measure and distinguish between fluorescence from 3-30 optically different fluorophore labels. That said, the aim with this project was to introduce a non-labeled MAP assay, as the introduction of fluorophore-labels can lead to alterations in the membrane interactions of MAPs [16–18].

2.5 Verifying our flow cytometry findings

To validate our observations from multi-parameter flow cytometry based on our chosen vesicle compositions, sizes, MAP:LV ratio and concentrations, we performed several complementary studies. This comparison is important, because certain MAPs can both permeabilize and solubilize vesicles [62]. Whether the former or later mechanism takes place depends on the concentrations of the MAP and lipids/LVs.

To support our core-fluorophore release data based on flow cytometry, we performed the traditional calcein release assay on calcein-containing LVs (cLVs), using the same total lipid and MAP concentrations as in our flow cytometry studies. The calcein release assay is a bulk measurement that relies on vesicles loaded with calcein in the aqueous core, which are in a quenched state due to the high local calcein concentration. When calcein is released from the core of the vesicles to the surroundings, the fluorescence signal from the calcein increases due to dequenching. In the calcein release assay, 0% calcein release refers to the fluorescence intensity of the bare cLVs, and 100% calcein release refers to the

fluorescence intensity for the cLVs solubilized by the Triton X-100 detergent. The calcein release was measured after 30 min. The calcein release (Figure 7A) and the core-fluorophore release derived from flow cytometry (Figure 5A) are very similar for magainin-2 and macrolittin-70. LL-37 and melittin show complete release, while no release was measured for Tat and penetratin (Figure 7A). These results are also well aligned with the flow cytometry data (Figure 5A). We also measured calcein release after 60 min and 120 min (Figure S8 in SI). We found that the calcein release data at 30-60 min were similar to data obtained at 120 min. Therefore, measuring the mixtures on the flow cytometer after 30-60 min appears to be at, or close to, a steady-state condition for all the MAPs. Together, we observed a good agreement between the membrane activities derived from the flow cytometry studies and the traditional calcein assay. That said, it should be noted that the flow cytometry assay provides information that is not accessible by the calcein assay, as it reveals the mechanisms behind the fluorophore leakage.

DLS data on the cLVs was used to investigate the integrity (with respect to size) of the cLVs upon MAP exposure in order to complement and verify the membrane fluorescence flow cytometry data. The magainin-2 and macrolittin-70 DLS data (Figure 7B) are consistent with the flow cytometry, which shows that the LVs are intact (Figure 5). In case of the LL-37, the DLS analysis gave rise to two size populations (Figure 7B). One smaller (11 ± 3 nm) and one larger (253 ± 124 nm) than the 152 ± 46 nm for the untreated cLVs. A DLS analysis based on particle-volume that is less biased towards the larger particles, which scatter much more than small particles (data presented in Figure 7B are based on the intensity-weighted analysis), showed that the population with the smaller size was the most abundant size-population (Figure S9A in SI). This is in good agreement with our flow cytometry findings, including the count rate and membrane fluorescence data: LL-37 dissolves the LVs and form micelles (too small to be detected by flow cytometry) and a few larger aggregates (detected by flow cytometry). The DLS data on the CPPs Tat and penetratin are more ambiguous. In case of Tat, two populations were observed, one with a size similar to unaffected vesicles, and another with a much larger size, and with a large variation, in line with potential vesicle aggregation taken place. This pattern is consistent for the DLS analysis based on volume (Figure S9B in SI). The two size populations of Tat probably occurred because only vesicles

with a sufficient amount of Tat bound are able to aggregate. The size of the cLVs exposed to penetratin indicates a slight increase compared to the non-treated cLVs, supporting the conclusion from flow cytometry that penetratin mediates vesicle aggregation/fusion.

Finally, we decided to perform a visual inspection of the proposed modes of action for the peptides by fluorescence microscopy. To do this, we prepared GUVs consisting of POPC, POPS and DOPE-Atto655 in a molar ratio of 79.5:20:0.5 (similar to the LV composition used for the flow cytometry studies) via electroformation using a sucrose solution for the formation protocol [53]. The GUVs were added to a glucose solution with 50 µM calcein in a BSA-passivated glass-bottom observation chamber. Lastly, the peptides were added and a time lapse recording was initiated with a temporal resolution of 15 sec. We employed LL-37, macrolittin-70, and Tat for this study, as they represent LV solubilization, permeabilization, and aggregation/fusion modes of action, respectively. The upper row of images in Figure 7C were recorded shortly after we added the MAPs to the observation chamber, while the images in the lower row show examples of how individual GUVs were modified due to their interaction with the MAPs at a later time point. It is clear that LL-37 solubilizes the GUV (within a 15 sec timeframe), and that macrolittin-70 permeabilizes the GUV, as the surrounding calcein diffuse into the GUV core. The macrolittin-70 treated GUVs were solubilized at a later time point (Table S1 in SI). This observation shows that certain MAPs are able to both introduce permeability and to solubilize vesicles depending on the MAP and lipid concentrations. In the case of Tat, aggregation was immediately observed after addition (Figure 7C, top row) and only increased over time (Figure 7C, bottom row). It is evident from these studies that Tat does not mediate permeabilization of the GUVs, as the surrounding calcein stays outside the GUVs. These images are representative for the GUVs observed, and statistics for the GUVs are shown in Table S1. The GUV-studies confirmed the three different modes of action triggered by LL-37, macrolittin-70, and Tat that were derived from the flow cytometry analysis.

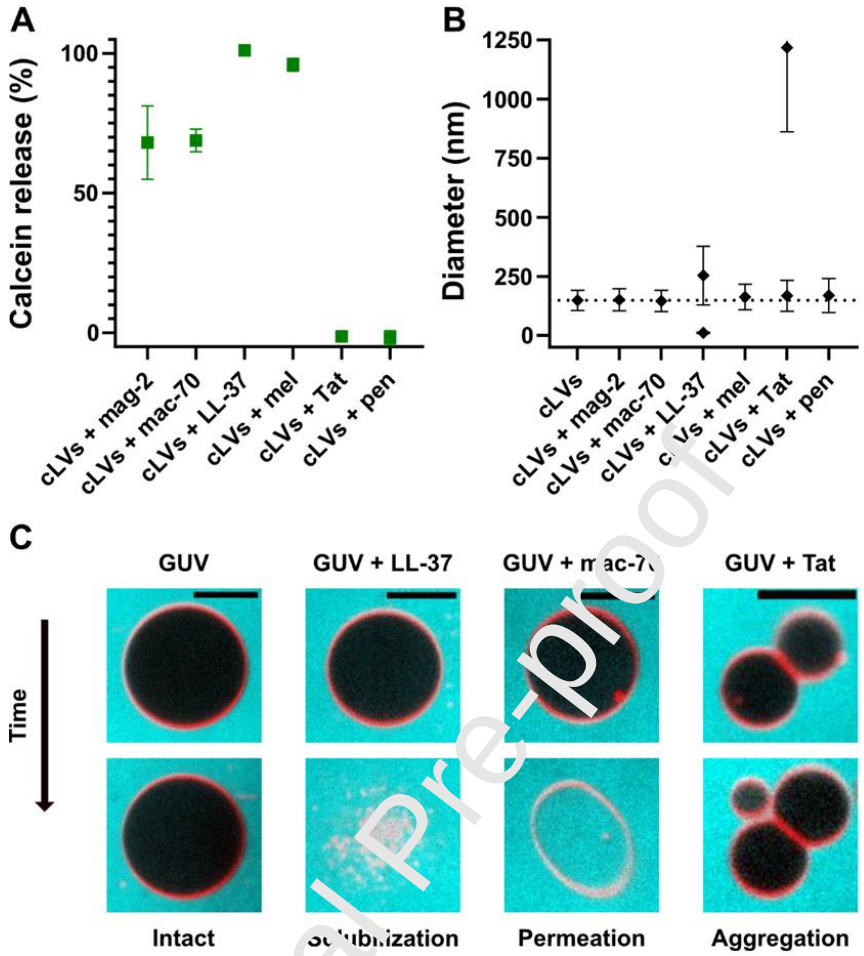

Figure 7. Complementary data to verify our flow cytometry findings. (A) MAP-induced calcein release from cLVs after 30 min. 0 % release is defined from the fluorescence intensity of bare cLVs, and 100% release is defined from the fluorescence intensity of cLVs solubilized by the Triton X-100 detergent. Each data point is the average of two independent measurements and their standard deviation. (B) Apparent diameter of cLVs in the presence of each of the MAPs as determined by DLS. Each data point represents the average of at least five measurements on two independent samples, and the corresponding standard deviation. The dotted line shows the bare cLVs. (C) MAP interactions with GUVs studied by fluorescence microscopy. Calcein is shown in cyan, and GUV membranes in red. A black GUV core indicates a tight non-leaking GUV membrane barrier. The first column from left displays a control GUV without peptide at 1:43 min:sec (top) and at 42:45 min:sec (bottom). The second column displays a GUV incubated with LL-37 at 6:40 min:sec (top) and at 6:55 min:sec (bottom). The third

column display a GUV incubated with macrolittin-70 at 3:31 min:sec (top) and at 4:16 min:sec (bottom). The fourth column displays a GUV incubated with Tat at 3:27 min:sec (top) and at 31:56 min:sec (bottom). Scale bar: 10 µm. mag-2: magainin-2, mac-70: macrolittin-70, mel: melittin, pen: penetratin.

To sum up, the complementary studies, including the calcein release assay, DLS, and fluorescence microscopy on GUVs, support our flow cytometry findings, and thus verify that flow cytometry is a powerful technique to reveal how peptides interact with vesicles. Key advantages of the flow cytometry assay over the traditional methods include: (i) The flow cytometry assay is a high-throughput assay, unlike microscopy, and allowed us to detect 1000-2000 individual vesicles per second with limited time spent on sample preparation; (ii) label-free peptides can be used in this assay; (iii) detailed information about some of the most common modes of action between peptides and lipid membranes can be derived from the multi-readouts from individual LVs. Several other readouts/parameters can be added to the flow cytometric assay, including light scattering and additional fluorescence signals/probes. Further, the effects of lipid composition of the LV-based membrane-model system and time on the peptide-lipid membrane interactions can be studied with the flow cytometry-based assay. Finally, a detailed analysis of the fluorescence histograms may also provide insights into whether leakage is of a graded or all-or-none type [64]. Thus, the flow cytometry assay displays many of the same strengths as previous advanced fluorescence-based assays developed in our laboratory [65,66], but with the added benefit of requiring less specialized equipment, simpler work procedures, and non-customized data analysis software.

3. Conclusions

We have shown that flow cytometry can be used to identify different modes of action between membrane-active peptides and lipid membranes. These modes of action include membrane permeabilization, solubilization, and vesicle aggregation/fusion. The different mechanisms derived from the flow cytometry studies were confirmed by a bulk calcein release assay, DLS, and fluorescence microscopy studies on GUVs. Some of the attractive features of the presented flow cytometric assay are that: (i) it is a high-throughput assay (~2000 particle/s) with limited time spent on sample preparation, (ii) it can measure

several parameters on single particles, including membrane-fluorophore fluorescence of LVs, core-fluorophore fluorescence of LVs and relative LV concentrations in our case, and (iii) flow cytometers are commonplace in many research laboratories, and thus accessible for many researchers. We believe that the flow cytometric assay presented here can be used for various types of peptide-membrane studies, e.g. to identify new antibiotics. Moreover, the assay can easily be expanded to derive additional valuable information.

4. Materials and methods

4.1 Materials

Calcein, sodium dihydrogen phosphate, sodium chloride (NaCl), dimethylformamide (DMF), piperidine, dichloromethane (DCM), trifluoroacetic acid (TFA), triisopropylsilane (TIPS), diethylether, acetonitrile (MeCN), resins (Fmoc-Ser(tBu)-Wang, Fmoc-Leu-Wang resin, Fmoc-Arg(Pbf)-Wang Fmoc-PAL-AM, TentaGel S RAM), bovine serum albumin (BSA) sucrose, D-(+)-glucose, phosphate buffered saline (PBS), and Triton X-100 were purchased from Sigma-Aldrich (St. Louis, MO, USA). Chloroform and methanol were purchased from VWR Chemicals (Radnor, PA, USA). 1-Palmitoyl-2-oleoyl-*sn*-glycero-3-phosphocholine (POPC) and 1-palmitoyl-2-oleoyl-*sn*-glycero-3-phospho-L-serine sodium salt (POPS) were purchased from Avanti Polar Lipids (Alabaster, AL, USA). 1,2-Dioleoyl-*sn*-glycero-3-phosphoethanolamine-Atto655 (DOPE-Atto655) was purchased from Atto-Tec (Siegen, Germany). Alexa Fluor 488 hydrazide (Alex. 488) was purchased from Thermo Fisher Scientific (Waltham, MA, USA). Slurry for preparing Sepharose CL-4B columns was purchased from GE Healthcare (Little Chalfont, UK). Econo-Column glass chromatography column (dimensions 1.5×20 cm) was purchased from Bio-Rad (Hercules, CA, USA). Q-Max syringe filters with 0.22-µm cellulose acetate filtration membranes were purchased from Frisenette (Knebel, Denmark). Standard fluorenylmethoxycarbonyl (Fmoc)-protected amino acids, ethyl (hydroxyimino)cyanoacetate potassium salt (Oxyma) and diisopropylcarbodiimide (DIC) were purchased from Iris-Biotech. Micro-slide 8 well glass bottom was purchased from Ibidi (Gräfelfing, Germany). All chemicals were of reagent grade.

4.2 Vesicle preparation

We prepared the LVs for flow cytometry by dissolving the lipids in neat chloroform, mixed in the molar ratios mentioned in Table 1. The organic solvent was removed under a gentle nitrogen flow. Residual solvent was removed by placing the samples in vacuum (0.2-0.5 mbar) for approximately 2 hrs. Phosphate buffer (10 mM sodium phosphate, 100 mM NaCl, pH 6.7), filtered through a 0.22 μm sterile filter, with or without 80 μM Alexa488, as stated in Table 1, was added to the lipids, and the resulting lipid suspension was vortexed gently every 5 min over a period of 30 min and then subjected to five freeze-thaw cycles by alternate placement in a 70 °C water bath and a liquid nitrogen bath. Subsequently, the lipid suspension was extruded five times through a 400-nm polycarbonate membrane (Whatman, GE Healthcare) using a mini-extruder (Avanti Polar Lipids). For vesicle preparations containing Alexa488, excess Alexa488 was removed from the vesicles by size-exclusion chromatography using a Sepharose CL-4B column (dimensions 1.5×20 cm) eluted with phosphate buffer at a flow rate of 1 mL/min. For column-purified vesicles, the vesicles were added to an Amicon Ultra-4 100 kDa centrifugal filter unit (Merck, Darmstadt, Germany) and concentrated by centrifuging at 2,000×g.

cLVs were also prepared. This was done using a protocol similar to that described above for Alexa488-containing vesicles, except that (i) initial dissolution of the lipids was done using chloroform:methanol (9:1 V/V ratio), (ii) hydration of the lipids was done using a calcein solution (60 mM calcein, 10 mM sodium phosphate, pH 6.7 prepared using Milli-Q water filtered using a 0.22 μm sterile filter), (iii) extrusion was done 21 times through a 100-nm polycarbonate membrane (Whatman).

GUVs were prepared via electroformation using a Digimess HUC65-00 FG100 function generator using a procedure modified from Wheaten *et al.* [67]. The lipids (POPC:POPS:DOPE-Atto655) were mixed in a 79.5:20:0.5 molar ratio in chloroform (See Table 1) for a final concentration of 1 mM and stored at minus 20 ºC until use. 20 μL of the chloroform solution was deposited equally on two platinum rods, which were connected to a custom-made Teflon support. Both the Teflon support and rods were kept in vacuum for at least 1 hr to ensure efficient removal of chloroform. The GUVs were then produced by immersing the rods into a 226 mM sucrose solution and applying an AC field. To produce high quality GUVs, a constant sine wave shaped peak-to-peak voltage of 3.5 V was used in combination with three different

frequency settings. First 10 Hz was used for 2 hrs, then 5 Hz for 10 min, and finally 1 Hz for 10 min. The GUVs were harvested using a 500 µL glass syringe (Hamilton Company, Giarmata, Romania), kept at room temperature and used within 48 hrs.

The phosphorus concentration of the LV and cLV samples was determined using inductively coupled plasma mass spectrometry (ICP-MS, done on an iCAP Q ICP-MS, Thermo Fischer Scientific). The phospholipid concentration was then estimated by subtracting the contribution of the 10 mM phosphate buffer. Hence, the lipid concentration presented above refers to the phospholipid concentration measured by ICP-MS.

Table 1: Name of vesicle formulation as used in this article, the corresponding lipid composition, fluorophore encapsulated in the core, and in which type of measurements the vesicles were used.

Sample name	Lipid composition (molar ratio)	Core-fluorophore	Measurement
Anionic LVs with core-fluorophore	POPC:POPS:DOPE-Atto655 (79:20:1)	80 µM Alexa488	Flow cytometry
Anionic LVs without core-fluorophore	POPC:POPS:DOPE-Atto655 (79:20:1)	No fluorophore	Flow cytometry
Neutral LVs with core-fluorophore	POPC:DOPE-Atto655 (99:1)	80 µM Alexa488	Flow cytometry
Neutral LVs without core-fluorophore	POPC:DOPE-Atto655 (99:1)	No fluorophore	Flow cytometry
cLVs	POPC:POPS (80:20)	60 mM calcein	Calcein release assay and DLS
GUVs	POPC:POPS:DOPE-Atto655 (79.5:20:0.5)	No fluorophore	Microscopy

4.3 Nanoparticle tracking analysis (NTA)

The samples under investigation were diluted to ~150 nM vesicles (concentration in terms of lipid) in 10 mM phosphate buffer. The NTA measurements were performed using a ZetaView Particle PMX-220 TWIN 488/640 nm (Particle Metrix, Meerbusch, Germany). For the light scattering-based tracking a 640 nm laser was used. This laser was also used to excite/track the LVs based on the fluorescence from the membrane-fluorophore, while a 488 nm laser was used to excite and track the LVs based on the fluorescence from the core-fluorophore. Camera sensitivity of 75, 90 and 85 % were used, respectively, and exposure times of 1/100 s, 1/70 s, and 1/100 s, respectively. The measurements were carried out at approximately 25˚C, for three cycles at 11 different positions, with a measurement rate of 30 frames/second. Data were analyzed using the ZetaView 8.04.02 software.

4.4 Synthesis and purification of MAPs

All peptides were synthesized at 0.2 mmol scale on a Biotage Initiator+ Alstra microwave-assisted peptide synthesizer using standard Fmoc-protected amino acids. Fmoc-deprotection was performed by addition of deprotection solution (20% piperidine in DMF, 0.1 M Oxyma) to the resin, heating at 75 °C for 2 min, drained and washed once with DMF. New deprotection solution was added, heating was repeated at 75 °C for 5 min, and the resin was drained and washed 5 times with DMF. Coupling of the amino acid was performed by addition of the required amino acid solution (5 eq. of Fmoc-amino acid, 5 eq. Oxyma in DMF, 0.3 M) and DIC solution (2 M DIC in DMF). The resin was heated at 75 °C for 10 min, drained and washed once with DMF, and the coupling was repeated. After the second coupling, the resin was washed 4 times with DMF. After deprotection of the final amino acid residue, the resin was washed 5 times with DMF, 5 times with DCM and dried by suction for 15 min. For arginine residues, the coupling times were 25 min and 5 min. For histidine residues the temperature was lowered to 50 °C.

The peptidyl-resin was suspended in cleavage cocktail (95% TFA, 2.5% water, 2.5% TIPS) for 1 to 4

hours. The peptide-cleavage mixture was filtered off, and precipitated in cold diethylether, centrifuged, decanted and triturated (twice). The crude peptides were purified on a Dionex Ultimate 3000 reverse phase-high performance liquid chromatography (RP-HPLC) system equipped with a RQ variable wavelength detector and an automated fraction collector using a Phenomenex Gemini NX 5u, C18, 110 Å, 250 mm x 30 mm column at a 20 mL/min flow rate. RP-HPLC gradients were run using a solvent system consisting of solution A (H_2O + 0.1% TFA) and B (MeCN + 0.1% TFA). Pure fractions were combined and lyophilized. The purified peptides were analyzed on a Shimadzu NexeraX2 RP-HPLC system equipped with Shimadzu LC-30AD pumps, a Shimadzu SIL-30AC autosampler, a CTO-20AC column oven and a Shimadzu PDA detector (monitoring at 214 nm and 280 nm) using a Waters XBridge BEH C18, 2.5 µm 3.0 x 150 mm XP column at a flow rate of 0.5 mL/min. RP-HPLC gradients were run using a gradient from 0% to 50% of solution B over 10 min. The pure peptides were characterized by mass spectrometry using either a Bruker matrix assisted laser desorption ionization time of flight mass spectrometry (MALDI-TOF-MS) Autoflex speed or on a Waters Acquity Ultra Performance UPLC equipped with a QDa detector and an Acquity UPLC BEH C18, 1.7 µm, 2.1 x 50 mm column.

4.4.1 Characterization of the MAPs

4.4.1.1 Magainin-2

The magainin-2 sequence H-GIGKFLHSAKKFGKAFVGEIMNS-OH was synthesized on a pre-loaded Fmoc-Ser(tBu)-Wang resin (loading 0.63 mmol/g) using the synthesis procedure described above. After cleavage for 1 h, precipitation and RP-HPLC purification (10-40% B over 40 min) the desired peptide was obtained in 4% yield (Nanodrop (A214)) and 95% purity (HPLC) (Figure S10 in SI). LC-MS (Electrospray ionization (ESI)) *m/z*: = $[M+5H]^{5+}$ = 494.4 (calcd. 494.4), $[M+4H]^{4+}$ = 617.8 (calcd. 617.7), $[M+3H]^{3+}$ = 823.2 (calcd. 823.3) (Figure S11 in SI).

4.4.1.2 Macrolittin-70

The macrolittin-70 sequence H-GIGEVLKELATLLPELQSWIKAAQQL-OH was synthesized on a pre-

loaded Fmoc-Leu-Wang resin (loading 0.70 mmol/g) using the synthesis procedure described above. After cleavage for 1 h, precipitation and RP-HPLC purification (15-80% B over 40 min) the desired peptide was obtained in 23% yield (Nanodrop (A280)) and 91% purity (HPLC) (Figure S12 in SI). MALDI-TOF-MS *m/z*: $[M+Na]^+$ = 2871.37 (calcd. 2871.35) (Figure S13 in SI).

4.4.1.3 LL-37

The LL-37 sequence H-LLGDFFRKSKEKIGKEFKRIVQRIKDFLRNLVPRTES-OH was synthesized on a pre-loaded Fmoc-Ser(tBu)-Wang resin (loading 0.63 mmol/g) using the synthesis procedure described above. After cleavage for 4 h, precipitation and RP-HPLC purification (20-50% B over 60 min) the desired peptide was obtained in 8% yield (Nanodrop (A214)) and 100% purity (HPLC) (Figure S14 in SI). MALDI-TOF-MS *m/z*: $[M+H]^+$ = 4493.28 (calcd. 4493.34) (Figure S15 in SI).

4.4.1.4 Melittin

The melittin sequence H-GIGAVLKVLTTGLPALISWIKRKRQQ-NH_2 was synthesized on TentaGel S RAM resin (loading 0.23 mmol/g) using the synthesis procedure described above. After cleavage for 4 h, precipitation and RP-HPLC purification (20-60% B over 40 min) the desired peptide was obtained in 4% yield (Nanodrop (A280)) and 99% purity (HPLC) (Figure S16 in SI). LC-MS (ESI) *m/z*: = $[M+6H]^{6+}$ = 475.4 (calcd. 475.4), $[M+5H]^{5+}$ = 569 (calcd. 570.3), $[M+4H]^{4+}$ = 712.3 (calcd. 712.6), $[M+3H]^{3+}$ = 949.7 (calcd. 949.8) (Figure S17 in SI).

4.4.1.5 Tat

The Tat sequence H-YGRKKRRQRRR-OH was synthesized on a pre-loaded Fmoc-Arg(Pbf)-Wang resin (loading 0.64 mmol/g) using the synthesis procedure described above. After cleavage in TFA-TIS-thioanisole-water (90%/2.5%/2.5%/5%) for 16 h, precipitation and RP-HPLC purification (1% B for 10 min then 1-50% over 33 min) the desired peptide was obtained in 3% yield (Nanodrop (A280)) and 99% purity (HPLC) (Figure S18 in SI). LC-MS (ESI) *m/z*: = $[M+5H]^{5+}$ = 312.9 (calcd. 313.0), $[M+4H]^{4+}$ = 391.1 (calcd. 391.0), $[M+3H]^{3+}$ = 521.1 (calcd. 521.0), $[M+2H]^{2+}$ = 780.5 (calcd. 780.9) (Figure S19 in SI).

4.4.1.6 Penetratin

The penetratin sequence H-RQIKIWFQNRRMKWKK-NH_2 was synthesized on Fmoc-PAL-AM resin (loading 0.61 mmol/g) using the synthesis procedure described above. After cleavage for 4 h, precipitation and RP-HPLC purification (10-40% B over 40 min) the desired peptide was obtained in 21% yield (Nanodrop (A280)) and 93% purity (HPLC) (Figure S20 in SI). Liquid chromatography-MS (LC-MS) (ESI) *m/z*: = $[M+5H]^{5+}$ = 450.3 (calcd. 450.2), $[M+4H]^{4+}$ = 562.4 (calcd. 562.6), $[M+3H]^{3+}$ = 749.5 (calcd. 749.6), $[M+2H]^{2+}$ = 1123.8 (calcd. 1123.9) (Figure S21 in SI).

4.4.2 Quantification of MAPs

The absorption spectrum of the solubilized MAPs was measured using a NanoDrop 2000c spectrophotometer (NanoDrop Products, Thermo Fisher Scientific), and the exact MAP concentrations were calculated using Lambert-Beer's law with the following extinction coefficients: macrolittin-70, 5,500 M^{-1} cm^{-1} at 280 nm; melittin, 5,500 M^{-1} cm^{-1} at 280 nm; Tat, 1,490 M^{-1} cm^{-1} at 280 nm; penetratin, 11,000 M^{-1} cm^{-1} at 280 nm; magainin-2, 42,783 M^{-1} cm^{-1} at 214 nm; LL-37, 58,639 M^{-1} cm^{-1} at 214 nm. The extinction coefficients for macrolittin-70, melittin, Tat, and penetratin were calculated using the work by Pace et al [68], and the extinction coefficients for magainin-2 and LL-37, which contains no tryptophans or tyrosines, were calculated using the work by Kuipers and Gruppen [69].

4.5 Handling of MAPs

Freeze-dried MAPs were adjusted to room temperature, and phosphate buffer, filtered using a 0.22 µm sterile filter, was added to obtain an approximate MAP concentration of 500 µM. The solutions were vortexed gently for 10 sec. The absorption spectrum of the solutions was then measured using a NanoDrop 2000c spectrophotometer, and the exact MAP concentrations were calculated using Lambert-Beer's law as described in section 4.4.2.

4.6 Flow cytometry

The effect of MAPs on vesicles were measured by adding MAPs to vesicles to a final MAP concentration

of 10 μM and a final lipid concentration of 50 μM. The solution was mixed by vortexing gently, and left to react for 30-60 min at 37˚C. Just before flow cytometry measurements, the solutions were diluted 100-fold to a final lipid concentration of 500 nM, and vortexed gently. Dilutions were done in phosphate buffer.

A BD LSRFortessa Flow cytometer (BD-Biosciences-US) was used to study fluorophore-labeled vesicles and their interactions with MAPs (See Table 1). BD CS&T quality and control beads were used prior to the experiments to standardize the performance of the equipment. The measurements were run with a low flow rate (1 μl/min). The events were triggered by the fluorescence from DOPE-Atto655 fluorescence at a trigger value of 200, using a 640 nm laser. The emission from the Atto655 was detected at 655-685 nm. Alexa488 was excited using a 488 nm laser, and the emission detected at 515-545 nm. The applied voltages were chosen based on the signal from the anionic LVs with core-fluorophore. The voltage for the Atto655 detector was set to 280 V to detect a significant proportion of vesicles (800-2400 events/s for untreated vesicles) relative to the number of events from the buffer (typically <1 event/s). The voltage for the Alexa488 detector was set to 460 V. This value gave a rise to a relevant dynamic range of Alexa488 fluorescence in which the Alexa488 (core-fluorophore) loaded were measurable and distinguishable from empty vesicles. For measurements triggered on the core fluorescence, the trigger value was 200, using the 488 nm laser. The applied voltages were the same as for measurements triggered by the fluorescence from DOPE-Atto655. Events were recorded to a total of 50,000 events or at least 120 sec, whichever came first.

The fluorescence intensities are reported by the height value from the recorded pulses because this has been reported to be the optimal read-out when studying submicron particles [70]. FlowJo v 10.7.2 was used to extract the median fluorescence intensities (MFIs) and the count rates and to generate the figures. All measurements were carried out at room temperature.

4.7 Calcein release assay

Stock samples with cLVs or MAPs were heated to 37 °C. The stock samples were mixed directly in black 96-well plates (Nunc, Thermo Fischer Scientific) to a final lipid concentration of 50 μM, a final MAP

concentration of 10 μM, and a final volume of 150 μl. The mixtures were incubated for 30, 60, or 120 min at 37 °C. The fluorescence emission intensity, F, was measured using a Spark multimode microplate reader (Tecan, Männedorf, Switzerland) with an excitation wavelength of 491 nm and an emission wavelength of 514 nm. The fluorescence emission intensity of intact cLVs, F_0, was measured using cLVs incubated without MAPs, and the fluorescence emission intensity for maximum calcein release, F_{max}, was measured using cLVs incubated with 0.5% Triton X-100. The calcein release was calculated using the equation

$$\text{Calcein release } (\%) = \frac{F - F_0}{F_{max} - F_0} \times 100\%.$$

4.8 Dynamic light scattering (DLS)

cLVs were mixed with MAPs to a final lipid concentration of 50 μM and a final MAP concentration of 10 μM. The samples were incubated for 30-60 min at 37 °C before investigation by DLS using a Zetasizer Nano ZS (Malvern, Worcestershire, UK). The DLS measurements were performed at 37 °C. The number of runs per measurement were adjusted automatically by the Zetasizer. The acquired data were evaluated using an intensity-based size distribution analysis. Sizes representing ≤2 % of the total intensity were not included in the final data representation. In a few cases, the volume-weighted size distributions were also presented.

4.9 Microscopy and image analysis

Imaging of GUVs was performed using a Nikon Ti2, Yokogawa CSU-W1 spinning disc confocal microscope equipped with a high numerical aperture 60x oil immersion objective and a Photometrics Prime 95B sCMOS detector. The images were acquired by alternating between exciting calcein and DOPE-Atto655 using 488 nm and 638 nm diode laser lines, respectively. The calcein emission was passed through a 520/28 Brightline HC filter set, while DOPE-Atto655 was passed through 600/50 ET Bandpass filter set. Ibidi micro-slide 8 wells were passivated with BSA by incubating 300 μl 1 g/l BSA in PBS in each well for a minimum of 30 min before washing each well 8 times with a 300 μL 226 mM glucose solution. The BSA passivated micro-slides were inserted into the microscope. 150 μl of a 226

mM glucose solution containing 50 μM calcein was added to the chamber. 25 μl of the GUV solution was hereafter added and incubated for 2 min before adding 150 μL 226 mM glucose solution containing both 50 μM calcein and peptide. The final peptide concentration was 50 μM and the final calcein concentration was 46 μM. Imaging was performed for a minimum of 30 min and was initiated immediately after the last solution was added to the chamber. A temporal resolution of 15 sec was applied. Presented images were sectioned and edited for brightness and contrast in ImageJ.

5. Acknowledgement

We thank Bente Rotbøl for technical assistance with the flow cytometer and Jaco Botha and Nicolai Paulsen for critical reading of the manuscript. The work presented in this article is supported by Novo Nordisk Foundation grant NNF16OC0022166.

6. References

[1] K. Matsuzaki, S. Yoneyama, K. Miyajima, Pore formation and translocation of melittin, Biophys. J. 73 (1997) 831–838. https://doi.org/10.1016/S0006-3495(97)78115-3.

[2] L. Gentilucci, A. Tolomelli, F. Squassabia, Peptides and Peptidomimetics in Medicine, Surgery and Biotechnology, Curr. Med. Chem. 13 (2006) 2449–2466. https://doi.org/10.2174/092986706777935041.

[3] S. Li, S.Y. Kim, A.E. Pittman, G.M. King, W.C. Wimley, K. Hristova, Potent Macromolecule-Sized Poration of Lipid Bilayers by the Macrolittins, A Synthetically Evolved Family of Pore-Forming Peptides, J. Am. Chem. Soc. 140 (2018) 6441–6447. https://doi.org/10.1021/jacs.8b03026.

[4] W.C. Wimley, K. Hristova, Antimicrobial peptides: Successes, challenges and unanswered questions, J. Membr. Biol. 239 (2011) 27–34. https://doi.org/10.1007/s00232-011-9343-0.

[5] J. Xie, Y. Bi, H. Zhang, S. Dong, L. Teng, R.J. Lee, Z. Yang, Cell-Penetrating Peptides in Diagnosis and Treatment of Human Diseases: From Preclinical Research to Clinical Application, Front. Pharmacol. 11 (2020) 697. https://doi.org/10.3389/fphar.2020.00697.

[6] Y. Li, H. Wu, P. Teng, G. Bai, X. Lin, X. Zuo, C. Cao, J. Cai, Helical Antimicrobial Sulfono-γ-AApeptides, J. Med. Chem. 58 (2015) 4802–4811. https://doi.org/10.1021/acs.jmedchem.5b00537.

[7] M.K. Kim, N. Kang, S.J. Ko, J. Park, E. Park, D.W. Shin, S.H. Kim, S.A. Lee, J.I. Lee, S.H. Lee, E.G. Ha, S.H. Jeon, Y. Park, Antibacterial and antibiofilm activity and mode of action of magainin 2 against drug-

resistant acinetobacter baumannii, Int. J. Mol. Sci. 19 (2018). https://doi.org/10.3390/ijms19103041.

[8] J.H. Choi, A.Y. Jang, S. Lin, S. Lim, D. Kim, K. Park, S.M. Han, J.H. Yeo, H.S. Seo, Melittin, a honeybee venom-derived antimicrobial peptide, may target methicillin-resistant Staphylococcus aureus, Mol. Med. Rep. 12 (2015) 6483–6490. https://doi.org/10.3892/mmr.2015.4275.

[9] Y. Huan, Q. Kong, H. Mou, H. Yi, Antimicrobial Peptides: Classification, Design, Application and Research Progress in Multiple Fields, Front. Microbiol. (2020). https://doi.org/10.3389/fmicb.2020.582779.

[10] S. Macchi, G. Signore, C. Boccardi, C. Di Rienzo, F. Beltram, F. Cardarelli, Spontaneous membrane-translocating peptides: influence of peptide self-aggregation and cargo polarity., Sci. Rep. 5 (2015) 16914. https://doi.org/10.1038/srep16914.

[11] A. Dinca, W.-M. Chien, M. Chin, Intracellular Delivery of Proteins with Cell-Penetrating Peptides for Therapeutic Uses in Human Disease, Int. J. Mol. Sci. 17 (2016) 263. https://doi.org/10.3390/ijms17020263.

[12] H. Wang, J. Ma, Y. Yang, F. Zeng, C. Liu, Highly Efficient Delivery of Functional Cargoes by a Novel Cell-Penetrating Peptide Derived from SP140-Like Protein, Bioconjug. Chem. 27 (2016) 1373–1381. https://doi.org/10.1021/acs.bioconjchem.6b00161.

[13] E.J.B. Nielsen, S. Yoshida, N. Kamei, R. Iwanage, E.S. Khafagy, J. Olsen, U.L. Rahbek, B.L. Pedersen, K. Takayama, M. Takeda-Morishita, In vivo proof of concept of oral insulin delivery based on a co-administration strategy with the cell-penetrating peptide penetratin, J. Control. Release. 189 (2014) 19–24. https://doi.org/10.1016/j.jconrel.2014.06.022.

[14] M. Kristensen, H.M. Nielsen, Cell-penetrating peptides as tools to enhance non-injectable delivery of biopharmaceuticals, Tissue Barriers. 4 (2016). https://doi.org/10.1080/21688370.2016.1178369.

[15] J.B. Larsen, N. Taebnia, A. Dolatshahi-Pirouz, A.Z. Eriksen, C. Hjørringgaard, K. Kristensen, N.W. Larsen, N.B. Larsen, R. Marie, A.-K. Mündler, L. Parhamifar, A.J. Urquhart, A. Weller, K.I. Mortensen, H. Flyvbjerg, T.L. Andresen, Imaging therapeutic peptide transport across intestinal barriers, RSC Chem. Biol. (2021). https://doi.org/10.1039/d1cb00024a.

[16] S.F. Hedegaard, M.S. Derbas, T.K. Lind, M.R. Kasimova, M.V. Christensen, M.H. Michaelsen, R.A. Campbell, L. Jorgensen, H. Franzyk, M. Cárdenas, H.M. Nielsen, Fluorophore labeling of a cell-penetrating peptide significantly alters the mode and degree of biomembrane interaction, Sci. Rep. 8 (2018) 1–14. https://doi.org/10.1038/s41598-018-24154-z.

[17] L.D. Hughes, R.J. Rawle, S.G. Boxer, Choose your label wisely: Water-soluble fluorophores often interact with lipid bilayers, PLoS One. 9 (2014) e87649. https://doi.org/10.1371/journal.pone.0087649.

[18] Z. Zhang, D. Yomo, C. Gradinaru, Choosing the right fluorophore for single-molecule fluorescence studies in a lipid environment, Biochim. Biophys. Acta - Biomembr. 1859 (2017) 1242–1253. https://doi.org/10.1016/j.bbamem.2017.04.001.

[19] G. Van Den Bogaart, J.V. Guzmán, J.T. Mika, B. Poolman, On the mechanism of pore formation by melittin, J. Biol. Chem. 283 (2008) 33854–33857. https://doi.org/10.1074/jbc.M805171200.

[20] S. Rex, Pore formation induced by the peptide melittin in different lipid vesicle membranes, Biophys. Chem. 58 (1996) 75–85. https://doi.org/10.1016/0301-4622(95)00087-9.

[21] R.M. Epand, R.F. Epand, Liposomes as Models for Antimicrobial Peptides, Methods Enzymol. 372 (2003) 124–133. https://doi.org/10.1016/S0076-6879(03)72007-2.

[22] C. Kayalar, N. Düzgüneçs, Membrane action of colicin E1: detection by the release of carboxyfluorescein and calcein from liposomes, BBA - Biomembr. 860 (1986) 51–56. https://doi.org/10.1016/0005-2736(86)90497-9.

[23] S. Guha, J. Ghimire, E. Wu, W.C. Wimley, Mechanistic Landscape of Membrane-Permeabilizing Peptides, Chem. Rev. 119 (2019) 6040–6085. https://doi.org/10.1021/acs.chemrev.8b00520.

[24] K. Kristensen, J.R. Henriksen, T.L. Andresen, Applying fluorescence correlation spectroscopy to investigate peptide-induced membrane disruption, in: Methods Mol. Biol., Humana Press Inc., 2017: pp. 159–180. https://doi.org/10.1007/978-1-4939-6737-7_11.

[25] R. Rathinakumar, W.C. Wimley, Biomolecular Engineering by Combinatorial Design and High-Throughput Screening: Small, Soluble Peptides That Permeabilize Membranes, J. Am. Chem. Soc. 130 (2008) 9849–9858. https://doi.org/10.1021/ja8017863.

[26] A.L. Russell, A.M. Kennedy, A.M. Spuches, D. Venugopal, J.B. Bhonsle, R.P. Hicks, Spectroscopic and thermodynamic evidence for antimicrobial peptide membrane selectivity, Chem. Phys. Lipids. 163 (2010) 488–497. https://doi.org/10.1016/J.CHEMPHYSLIP.2010.03.009.

[27] W.C. Wimley, Determining the effects of membrane-interacting peptides on membrane integrity, in: Cell-Penetrating Pept. Methods Protoc., 2015. https://doi.org/10.1007/978-1-4939-2806-4_6.

[28] H. Shaphiro, Practical Flow Cytometry Fourth Edition, A John Wiley Sons, Inc. Publ. (2003).

[29] J.M. Freire, D. Gaspar, B.G. De La Torre, A.S. Veiga, D. Andreu, M.A.R.B. Castanho, Monitoring antibacterial permeabilization in real time using time-resolved flow cytometry, Biochim. Biophys. Acta - Biomembr. (2015). https://doi.org/10.1016/j.bbamem.2014.11.001.

[30] S.G. Patel, E.J. Sayers, L. He, R. Narayan, T.L. Williams, E.M. Mills, R.K. Allemann, L.Y.P. Luk, A.T. Jones, Y.H. Tsai, Cell-penetrating peptide sequence and modification dependent uptake and subcellular distribution of green florescent protein in different cell lines, Sci. Rep. (2019). https://doi.org/10.1038/s41598-019-42456-8.

[31] J.B. Simonsen, E.B. Kromann, Pitfalls and opportunities in quantitative fluorescence-based nanomedicine studies – A commentary, J. Control. Release. (2021). https://doi.org/10.1016/j.jconrel.2021.05.041.

[32] K. Temmerman, W. Nickel, A novel flow cytometric assay to quantify interactions between proteins and membrane lipids, J. Lipid Res. (2009). https://doi.org/10.1194/jlr.D800043-JLR200.

[33] J.B. Simonsen, A liposome-based size calibration method for measuring microvesicles by flow cytometry, J. Thromb. Haemost. (2016). https://doi.org/10.1111/jth.13176.

[34] J.B. Simonsen, J.B. Larsen, C. Hempel, N. Eng, A. Fossum, T.L. Andresen, Unique Calibrators Derived from Fluorescence-Activated Nanoparticle Sorting for Flow Cytometric Size Estimation of Artificial Vesicles: Possibilities and Limitations, Cytom. Part A. 95 (2019). https://doi.org/10.1002/cyto.a.23797.

[35] S. Rex, Pore formation induced by the peptide melittin in different lipid vesicle membranes, Biophys. Chem. (1996). https://doi.org/10.1016/0301-4622(95)00087-9.

[36] Z. Yang, H. Choi, J.C. Weisshaar, Melittin-Induced Permeabilization, Re-sealing, and Re-permeabilization of E. coli Membranes, Biophys. J. (2018). https://doi.org/10.1016/j.bpj.2017.10.046.

[37] K. Matsuzaki, O. Murase, K. Miyajima, Kinetics of Pore Formation by an Antimicrobial Peptide, Magainin 2, in Phospholipid Bilayers, Biochemistry. (1995). https://doi.org/10.1021/bi00039a009.

[38] Y. Imura, N. Choda, K. Matsuzaki, Magainin 2 in action: Distinct modes of membrane permeabilization in living bacterial and mammalian cells, Biophys. J. (2008). https://doi.org/10.1529/biophysj.108.133488.

[39] U.H.N. Dürr, U.S. Sudheendra, A. Ramamoorthy, LL-37, the only human member of the cathelicidin family of antimicrobial peptides, Biochim. Biophys. Acta - Biomembr. (2006). https://doi.org/10.1016/j.bbamem.2006.03.030.

[40] D. Persson, P.E.G. Thorén, M. Herner, P. Lincoln, B. Nordén, Application of a novel analysis to measure

the binding of the membrane-translocating peptide penetratin to negatively charged liposomes, Biochemistry. (2003). https://doi.org/10.1021/bi026453t.

[41] E. Dupont, A. Prochiantz, A. Joliot, Penetratin Story: An Overview, in: Methods Mol. Biol., 2015: pp. 29–37. https://doi.org/10.1007/978-1-4939-2806-4_2.

[42] I.M. Kaplan, J.S. Wadia, S.F. Dowdy, Cationic TAT peptide transduction domain enters cells by macropinocytosis, J. Control. Release. (2005). https://doi.org/10.1016/j.jconrel.2004.10.018.

[43] C. Ciobanasu, J. Peter Siebrasse, U. Kubitscheck, Cell-penetrating HIV1 TAT peptides can generate pores in model membranes, Biophys. J. (2010). https://doi.org/10.1016/j.bpj.2010.03.065.

[44] E. Sancho-Vaello, P. François, E.J. Bonetti, H. Lilie, S. Finger, F. Gil-Ortiz, D. Gil-Carton, K. Zeth, Structural remodeling and oligomerization of human cathelicidin on membranes suggest fibril-like structures as active species, Sci. Rep. 7 (2017). https://doi.org/10.1038/s41598-017-14206-1.

[45] A.S. Ladokhin, S.H. White, "Detergent-like" permeabilization of anionic lipid vesicles by melittin, Biochim. Biophys. Acta - Biomembr. 1514 (2001) 253–260. https://doi.org/10.1016/S0005-2736(01)00382-0.

[46] J.B. Simonsen, J.B. Larsen, C. Hempel, N. Eng, A. Fossum, T.L. Andresen, Unique Calibrators Derived from Fluorescence-Activated Nanoparticle Sorting for Flow Cytometric Size Estimation of Artificial Vesicles: Possibilities and Limitations, Cytom. Part A. (2019). https://doi.org/10.1002/cyto.a.23797.

[47] S.A. Stoner, E. Duggan, D. Condello, A. Guerrero, J.R. Turk, P.K. Narayanan, J.P. Nolan, High sensitivity flow cytometry of membrane vesicles, Cytom. Part A. 89 (2016) 196–206. https://doi.org/10.1002/cyto.a.22787.

[48] A. Wagner, K. Vorauer-Uhl, Liposome Technology for Industrial Purposes, J. Drug Deliv. (2011). https://doi.org/10.1155/2011/591325.

[49] A.R. Karow, J. Götzl, P. Garidel, Resolving power of dynamic light scattering for protein and polystyrene nanoparticles, Pharm. Dev. Technol. (2015). https://doi.org/10.3109/10837450.2014.910808.

[50] V. Filipe, A. Hawe, W. Jiskoot, Critical evaluation of nanoparticle tracking analysis (NTA) by NanoSight for the measurement of nanoparticles and protein aggregates, Pharm. Res. (2010). https://doi.org/10.1007/s11095-010-0073-2.

[51] W. Anderson, D. Kozak, V.A. Coleman, Å.K. Jämting, M. Trau, A comparative study of submicron particle sizing platforms: Accuracy, precision and resolution analysis of polydisperse particle size distributions, J.

Colloid Interface Sci. (2013). https://doi.org/10.1016/j.jcis.2013.02.030.

[52] K.B. Johnsen, J.M. Gudbergsson, T.L. Andresen, J.B. Simonsen, What is the blood concentration of extracellular vesicles? Implications for the use of extracellular vesicles as blood-borne biomarkers of cancer, Biochim. Biophys. Acta - Rev. Cancer. 1871 (2019) 109–116. https://doi.org/10.1016/j.bbcan.2018.11.006.

[53] A.H. Kunding, M.W. Mortensen, S.M. Christensen, D. Stamou, A fluorescence-based technique to construct size distributions from single-object measurements: Application to the extrusion of lipid vesicles, Biophys. J. (2008). https://doi.org/10.1529/biophysj.108.128819.

[54] J.A. Welsh, E. Van Der Pol, G.J.A. Arkesteijn, M. Bremer, A. Brisson, E. Coumans, F. Dignat-George, E. Duggan, I. Ghiran, B. Giebel, A. Görgens, A. Hendrix, R. Lacroix, J. Lannigan, S.F.W.M. Libregts, E. Lozano-Andrés, A. Morales-Kastresana, S. Robert, L. De Rond, T. Tertel, J. Tigges, O. De Wever, X. Yan, R. Nieuwland, M.H.M. Wauben, J.P. Nolan, J.C. Jones, MIFlowCyt-EV: a framework for standardized reporting of extracellular vesicle flow cytometry experiments, J. Extracell. Vesicles. 9 (2020). https://doi.org/10.1080/20013078.2020.1713526.

[55] S.L. Pedersen, A.P. Tofteng, L. Malik, K.J. Jensen, Microwave heating in solid-phase peptide synthesis, Chem. Soc. Rev. 41 (2012) 1826–1844. https://doi.org/10.1039/c1cs15214a.

[56] G. Sessa, J.H. Freer, G. Colacicco, G. Weissmann, Interaction of alytic polypeptide, melittin, with lipid membrane systems., J. Biol. Chem. 244 (1969) 3575–3582. https://doi.org/10.1016/s0021-9258(18)83408-1.

[57] J.E. Cummings, T.K. Vanderlick, Aggregation and hemi-fusion of anionic vesicles induced by the antimicrobial peptide cryptdin-4, Biochim. Biophys. Acta - Biomembr. (2007). https://doi.org/10.1016/j.bbamem.2007.04.016.

[58] M.L. Jobin, P. Bonnafous, H. Temsamani, F. Dole, A. Grélard, E.J. Dufourc, I.D. Alves, The enhanced membrane interaction and perturbation of a cell penetrating peptide in the presence of anionic lipids: Toward an understanding of its selectivity for cancer cells, Biochim. Biophys. Acta - Biomembr. (2013). https://doi.org/10.1016/j.bbamem.2013.02.008.

[59] K. Matsuzaki, O. Murase, N. Fujii, K. Miyajima, Translocation of a Channel-Forming Antimicrobial Peptide, Magainin 2, across Lipid Bilayers by Forming a Pore, 1995.

[60] K.T. Nguyen, S. V. Le Clair, S. Ye, Z. Chen, Molecular interactions between magainin 2 and model membranes in situ, J. Phys. Chem. B. (2009). https://doi.org/10.1021/jp904154w.

[61] Y. Tamba, M. Yamazaki, Magainin 2-induced pore formation in the lipid membranes depends on its concentration in the membrane interface, J. Phys. Chem. B. (2009). https://doi.org/10.1021/jp8109622.

[62] J.R. Henriksen, T.L. Andresen, Thermodynamic profiling of peptide membrane interactions by isothermal titration calorimetry: A search for pores and micelles, Biophys. J. (2011). https://doi.org/10.1016/j.bpj.2011.05.047.

[63] J.E. Faust, P.Y. Yang, H.W. Huang, Action of Antimicrobial Peptides on Bacterial and Lipid Membranes: A Direct Comparison, Biophys. J. (2017). https://doi.org/10.1016/j.bpj.2017.03.003.

[64] S. Braun, Š. Pokorná, R. Šachl, M. Hof, H. Heerklotz, M. Hoernke, Biomembrane Permeabilization: Statistics of Individual Leakage Events Harmonize the Interpretation of Vesicle Leakage, ACS Nano. (2018). https://doi.org/10.1021/acsnano.7b08184.

[65] K. Kristensen, J.R. Henriksen, T.L. Andresen, Quantification of leakage from large unilamellar lipid vesicles by fluorescence correlation spectroscopy, Biochim. Biophys. Acta - Biomembr. (2014). https://doi.org/10.1016/j.bbamem.2014.08.007.

[66] K. Kristensen, N. Ehrlich, J.R. Henriksen, T.L. Andresen, Single-vesicle detection and analysis of peptide-induced membrane permeabilization, Langmuir. (2015). https://doi.org/10.1021/la504752u.

[67] S.A. Wheaten, F.D.O. Ablan, B.L. Spaller, J.M. Trieu, P.F. Almeida, Translocation of Cationic Amphipathic Peptides across the Membranes of Pure Phospholipid Giant Vesicles, J. Am. Chem. Soc. 135 (2013) 16517–16525. https://doi.org/10.1021/ja407451c.

[68] C.N. Pace, F. Vajdos, L. Fee, G. Grimsley, T. Gray, How to measure and predict the molar absorption coefficient of a protein, Protein Sci. 4 (1995) 2411–2423. https://doi.org/10.1002/pro.5560041120.

[69] B.J.H. Kuipers, H. Gruppen, Prediction of Molar Extinction Coefficients of Proteins and Peptides Using UV Absorption of the Constituent Amino Acids at 214 nm To Enable Quantitative Reverse Phase High-Performance Liquid Chromatography−Mass Spectrometry Analysis, (2007). https://doi.org/10.1021/jf070337l.

[70] P. Poncelet, S. Robert, N. Bailly, F. Garnache-Ottou, T. Bouriche, B. Devalet, J.H. Segatchian, P. Saas, F. Mullier, Tips and tricks for flow cytometry-based analysis and counting of microparticles, Transfus. Apher. Sci. (2015). https://doi.org/10.1016/j.transci.2015.10.008.

Declaration of competing interests

☒ The authors declare that they have no known competing financial interests or personal relationships that could have appeared to influence the work reported in this paper.

☐ The authors declare the following financial interests/personal relationships which may be considered as potential competing interests:

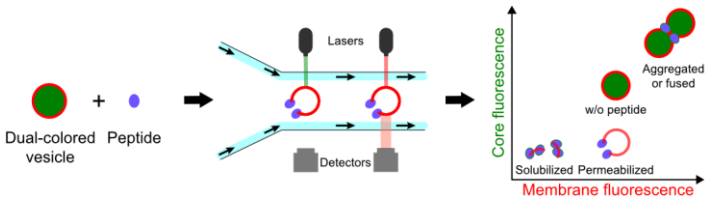

Graphical abstract

Highlights

- Developed a novel assay to study the modes of action of membrane-active peptides
- Our flow cytometric high-throughput assay rely on label-free peptides
- Fluorescence microscopy, DLS and calcein release studies confirmed the validity of our assay
- Six very different membrane-active peptides were evaluated in our assay

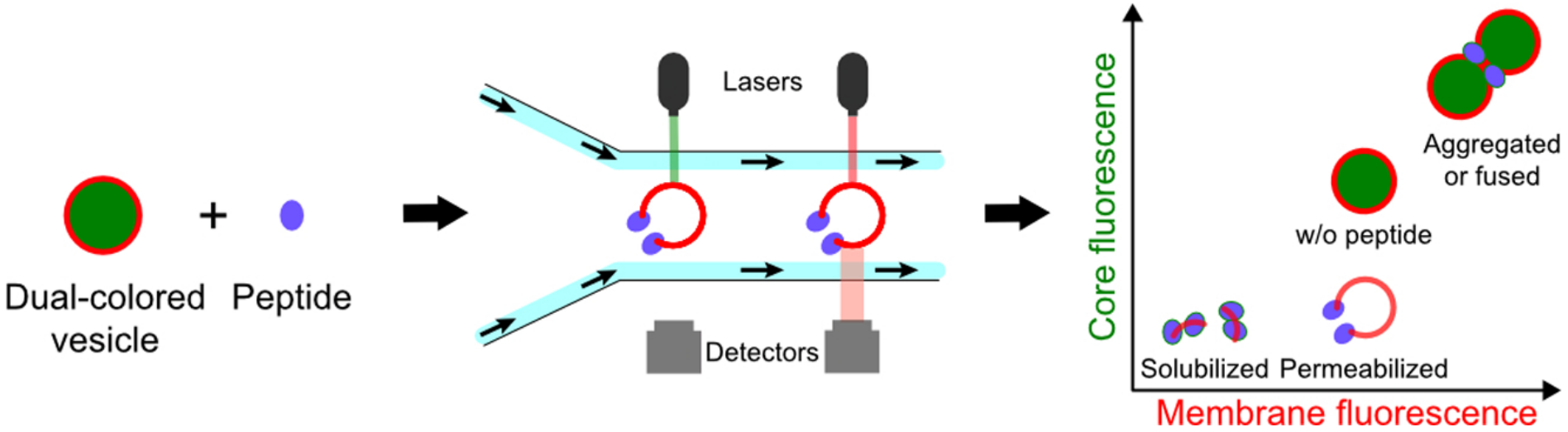

Graphics Abstract

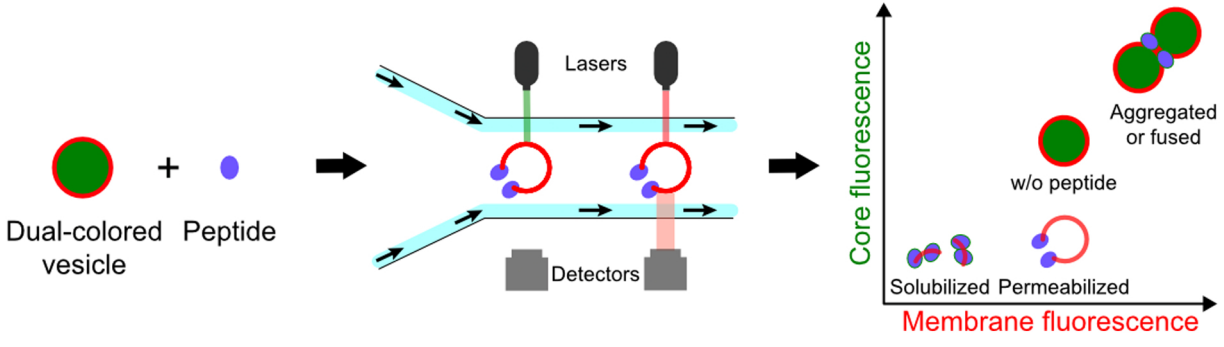
Dual-colored vesicle
Peptide
Lasers
Detectors
Core fluorescence
Aggregated or fused
w/o peptide
Solubilized
Permeabilized
Membrane fluorescence

Figure 1

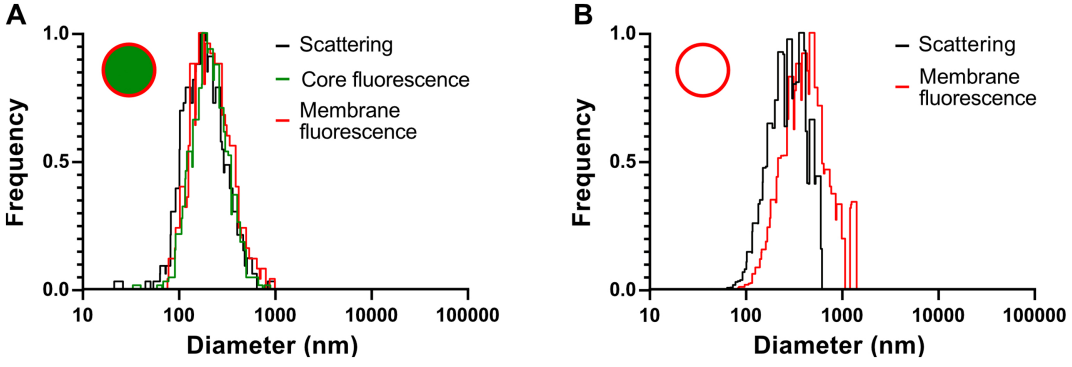
A
1.0
0.5
0.0
Frequency
Scattering
Core fluorescence
Membrane fluorescence
10
100
1000
10000
100000
Diameter (nm)
B
1.0
0.5
0.0
Frequency
Scattering
Membrane fluorescence
10
100
1000
10000
100000
Diameter (nm)

Figure 2

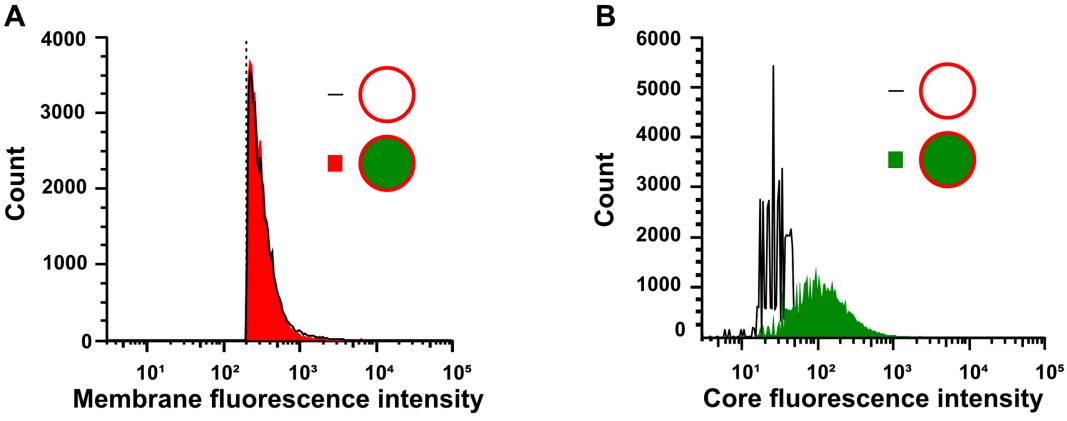
A
4000
3000
2000
1000
0
Count
10^1
10^2
10^3
10^4
10^5
Membrane fluorescence intensity
B
6000
5000
4000
3000
2000
1000
0
Count
10^1
10^2
10^3
10^4
10^5
Core fluorescence intensity

Figure 3

Magainin-2

Macrolittin-70

LL-37

Melittin

Tat

Penetratin

Figure 4

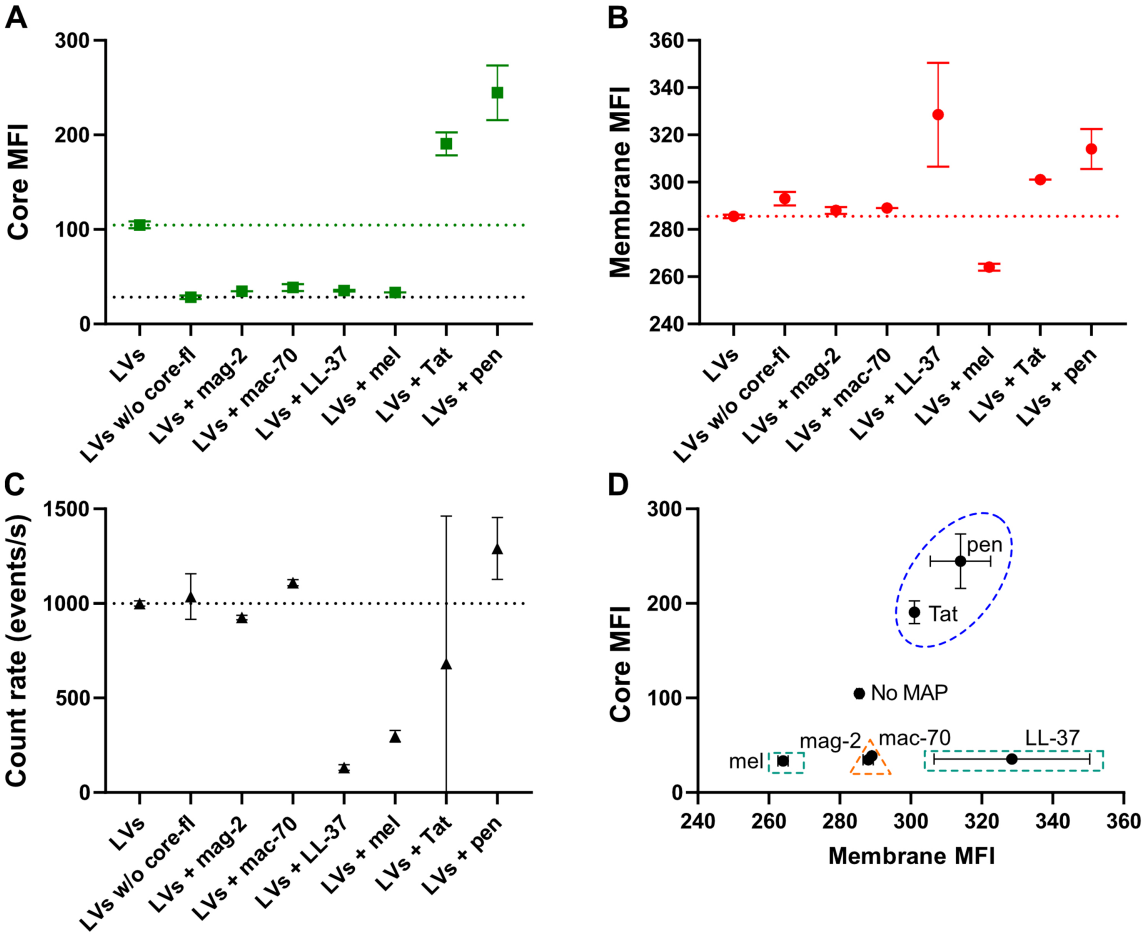
A
Core MFI
300
200
100
0
LVs
LVs w/o core-fl
LVs + mag-2
LVs + mac-70
LVs + LL-37
LVs + mel
LVs + Tat
LVs + pen
B
Membrane MFI
360
340
320
300
280
260
240
C
Count rate (events/s)
1500
1000
500
0
D
Core MFI
Membrane MFI
pen
Tat
No MAP
mag-2
mac-70
LL-37
mel

Figure 5

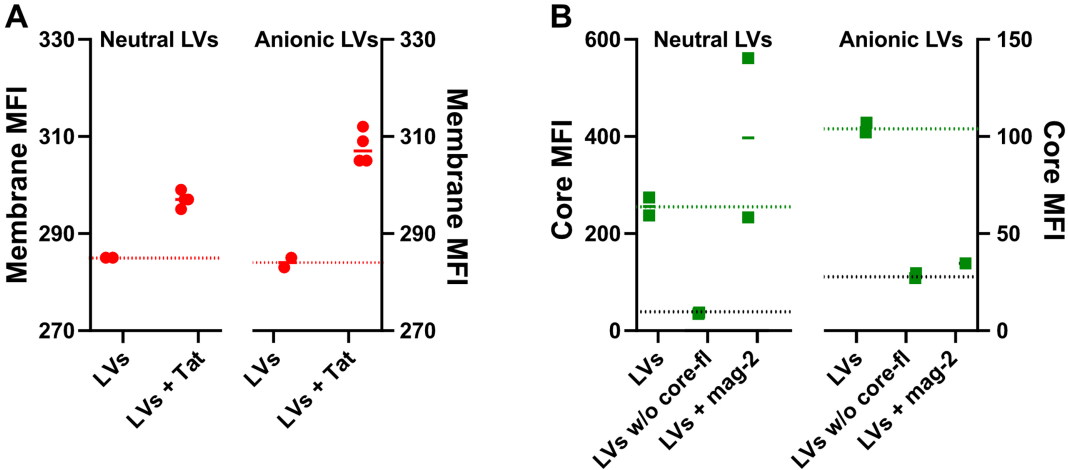
A
Neutral LVs
Anionic LVs
Membrane MFI
330
310
290
270
LVs
LVs + Tat
B
Neutral LVs
Anionic LVs
Core MFI
600
400
200
0
150
100
50
LVs
LVs w/o core-fl
LVs + mag-2

Figure 6

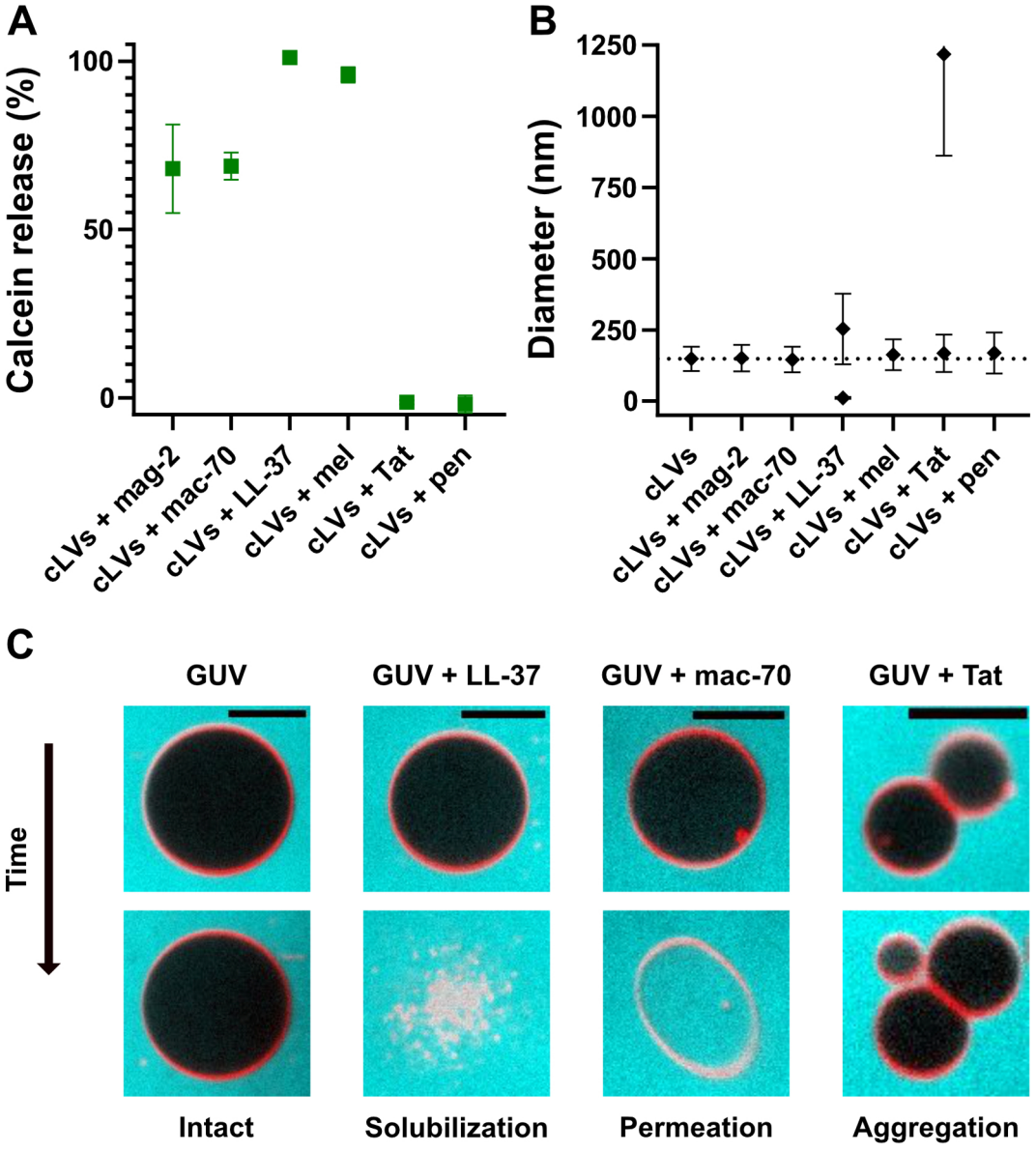
A
Calcein release (%)
100
50
0
cLVs + mag-2
cLVs + mac-70
cLVs + LL-37
cLVs + mel
cLVs + Tat
cLVs + pen
B
Diameter (nm)
1250
1000
750
500
250
0
cLVs
cLVs + mag-2
cLVs + mac-70
cLVs + LL-37
cLVs + mel
cLVs + Tat
cLVs + pen
C
GUV
GUV + LL-37
GUV + mac-70
GUV + Tat
Time
Intact
Solubilization
Permeation
Aggregation

Figure 7